Extended regulation interface coupled to the allosteric network and disease mutations in the PP2A-B56δ holoenzyme

Cheng-Guo Wu[1,2], Vijaya Kumar Balakrishnan[1], Pankaj Singh Parihar[1], Kirill Konovolov[3], Yu-Chia Chen[1,4], Ronald A Merrill[5], Hui Wei[6], Bridget Carragher[6], Ramya Sundaresan[1], Qiang Cui[7], Brian E. Wadzinski[8], Mark R. Swingle[9], Alla Musiyenko[9], Richard Honkanen[9], Aussie Suzuki[1,2,5], Stefan Strack[5], Xuhui Huang[3], Yongna Xing[1,2,*]

[1]McArdle Laboratory for Cancer Research, Department of Oncology, University of Wisconsin at Madison, School of Medicine and Public Health, Madison, Wisconsin 53705, USA

[2]Biophysics program, University of Wisconsin at Madison, Wisconsin 53706, USA

[3]Chemistry Department, University of Wisconsin at Madison, Wisconsin 53706, USA

[4]Molecular and Cellular Pharmacology program, University of Wisconsin at Madison, Wisconsin 53706, USA

[5]Department of Neuroscience and Pharmacology, University of Iowa, Iowa City, IA 52242, USA

[6]New York Structural biology Center, New York, NY 10027, USA

[7]Department of Chemistry, Metcalf Center for Science & Engineering, Boston University, Boston, MA 02215, USA

[8]Department of Pharmacology, Vanderbilt University, Nashville, TN 37232, USA

[9]Department of Biochemistry and Molecular Biology, University of South Alabama, Mobile, AL 36688, USA

[*]To whom correspondence should be addressed:

Yongna Xing
E-mail: xing@oncology.wisc.edu;
Phone: 608-262-8376
Fax: 608-262-2824

Abstract

An increasing number of mutations associated with devastating human diseases are being diagnosed by whole-genome/exon sequencing. Up to twenty *de novo* mutations have been discovered in B56δ (encoded by *PPP2R5D*), a regulatory subunit of protein phosphatase 2A (PP2A), that cause intellectual disabilities (ID) and a broad range of neurological symptoms. Single-particle cryo-EM structures show that the PP2A-B56δ holoenzyme possesses closed latent and open active forms. In the closed form, the long, disordered arms of B56δ termini fold against each other and the holoenzyme core, and establish dual autoinhibition of the phosphatase active site and the substrate-binding protein groove. The resulting interface spans over 190 Å and harbors unfavorable contacts, as well as activation phosphorylation sites and nearly all residues with ID-associated mutations. Our studies suggest that this super-dynamic interface is close to an allosteric network that is responsive to activation phosphorylation and is altered globally by ID mutations. We further showed that ID mutations perturbed the activation phosphorylation rates, mitotic progression, and mitotic error rates.

Introduction

Protein phosphatase 2A (PP2A) is a major serine/threonine phosphatase in the PPP family that targets many cellular phosphoproteins via diverse heterotrimeric holoenzymes in mammalian cells[1-6]. Each holoenzyme consists of a common core formed by the scaffolding A and catalytic C (PP2Ac) subunits, and a diverse regulatory subunit from one of the four major families (B/B55/PR55 (*PPP2R2*), B'/B56/PR61 (*PPP2R5*), B''/PR72 ((*PPP2R3*), and B'''/Striatin). Whole exome/genome sequencing identified a broad spectrum of disease mutations in PP2A subunits in cancer and neurological disorders[7-11]. Miscellaneous *de novo* mutations are associated with relatively rare diseases with unclear etiology. Both unique and shared mutations have been found in the common core of the B56 regulatory subunits. Up to 20 missense mutations in B56δ cause severe intellectual and developmental disorders[8,9,12,13] (https://jordansguardianangels.org), known as Jordan Syndrome. More recently, both severe and mild variants of Jordan syndrome have been associated with early-onset Parkinsonism[14-16]. Incidence of neurodevelopmental and neurodegenerative disorders associated with B56δ is estimated at 2.32 to 2.87 per 100,000 births; 250,000 cases are estimated to be undiagnosed[8,9,12,14-16].

Recent studies indicate that PP2A holoenzymes from the B56 family recognize a signature short linear motif (SLiM), LxxIxE, in the disordered regions of substrates[17-19]. Diverse SLiMs were found in intrinsically disordered regions that serve as docking interfaces for peptide-binding proteins and play crucial roles in modulating cellular signaling[20,21]. Several SLiMs have been uncovered for the PPP family phosphatases for targeting different substrates[22-25]. The B56-targeting LxxIxE SLiM binds to a protein groove in the conserved common core of B56 regulatory subunits[19,26]. Several thousands of B56 SLiM-containing proteins are predicted in the

human proteome and many of these are involved in broad cellular and physiological processes[17]. B56 regulatory subunits play essential roles in neurodevelopment, brain functions, and tumor suppression, as reflected by their ability to control cell cycle[17,18,27-29], cytoskeleton dynamics[30], DNA damage responses[31,32], CREB signaling[33], and c-Myc stability[34-38].

In addition to the common core, B56δ possesses long disordered regions at the N- and C-termini that are rich in phosphorylation sites (Extended Data Figs. 1-2). The PP2A-B56δ holoenzyme is known to be highly regulated by distinct cellular signaling pathways. Protein kinase A (PKA) phosphorylates B56δ and activates the holoenzyme, thereby regulating signaling molecules downstream of cyclic adenosine monophosphate (cAMP)[39-41]. At the G2/M checkpoint, the DNA-responsive checkpoint kinase Chk1 phosphorylates B56δ and stimulates the holoenzyme activity[42]. B56δ also plays a critical role in controlling mitotic exit[43]. Moreover, the B56δ holoenzyme is phosphorylated by the ataxia-telangiectasia mutated (ATM) kinase upon DNA damage and regulates p53 function[44]. The structure of the PP2A-B56δ holoenzyme and the structural basis of its activation are crucial for illuminating the complex regulation of this holoenzyme and the pathological mechanisms of its disease mutations.

Here we determined a high-resolution cryo-EM structure of a PP2A-B56δ holoenzyme bearing the E197K disease mutation at 2.7 Å. The structure resembles a closed form of the holoenzyme, in which the long N/C-extensions of B56δ make cross-arm interactions against each other and the holoenzyme core, creating an extended dynamic interface that suppresses both the phosphatase active site and the substrate SLiM-binding groove. Nearly all previously detected phosphorylation sites and residues mutated in patients with intellectual disabilities (ID) are located at or near this interface. We further demonstrated that ID mutations alter the activation

phosphorylation rates in response to cAMP-induced activation of PKA. ID muations also alter the basal level of SLiM-binding and up to a quarter of the key cellular signaling endpoints that affect cell cycle progression and the incidences of mitotic defects during cell division. Our studies reveal a coherent allosteric network crucial for B56δ holoenzyme activation upon phosphorylation that is altered globally by ID mutations.

Results

Overall cryo-EM structures of the PP2A-B56δ holoenzyme

Structure determination of the PP2A-B56δ holoenzyme by single-particle cryo-EM turned out to be highly challenging. We explored the "spotiton" technology[45,46] to capture the dynamic states of the holoenzyme on the grids. The spotiton grids "purified' a closed form of the holoenzyme by dissociating the majority of the holoenzyme particles (Extended data Fig. 3a). Albeit this form represents a small fraction of total particles, it gave a 4 Å map with uniform density for the long disordered regions at the N/C-termini (Extended data Fig. 3b). We further explored glutaraldehyde and EDC (ethyl carbodiimide) crosslinks and tested different detergents and EM grids to control ice thickness and particle behavior. Nonetheless, the cryo-EM data for the crosslinked holoenzyme failed to capture any closed forms. Next, we examined the holoenzyme bearing different ID mutations. After an extensive effort, we revealed two major forms for the E197K variant of the holoenzyme: a closed form with a map of 2.59 Å and a loose form with a map of 3.13 Å (Extended data Fig. 4). The crystal structure of the PP2A-B56γ1 holoenzyme (PDB code: 2NYL)[47,48], which represents the common core for the B56 family, fits the map for the B56δ holoenzyme core quite well. Since the N/C-arms are invisible in the loose form, we next focused on the structure of the closed form of the holoenzyme.

The building of the N/C-arms in the closed form was guided by XL-MS (crosslink mass spectrometry). Using zero-length EDC crosslink followed by multiple protease digestions and MS runs, two crosslinked residue pairs in the N/C-arms gave detection frequency comparable to or better than those in the holoenzyme core (Extended data Fig. 5). The structure of the closed form was refined at 2.7 Å (Extended data Table 1 and Extended data Fig. 4 and 6). It reveals extensive cross-arm interactions between the disordered regions of the B56δ termini; they interact with the holoenzyme core along a long path that spans over 190 Å (Fig. 1). While the long-distance line interface is intrinsically dynamic in nature, it also harbors a significant numer of unfavorable contacts (Fig. 1b), underlying an unprecedented super-long dynamic interface in this highly regulated holoenzyme.

The super-dynamic interface in the PP2A-B56δ holoenzyme

The above long-distance interface in the PP2A-B56δ holoenzyme is centered at the N/C-arm crossover that also makes close contacts with PP2Ac and the internal loop of B56 (B56-IL) (I) (Fig. 1b and Extended data Fig. 7a). The N/C-arms are juxtaposed against each other toward the termini and make close contacts with the B56δ core (II) (Fig. 1b and Extended data Fig. 7b). Diverging from the crossover and perpendicular to the juxtaposed lower N/C-arms, the upper C-arm makes rich hydrophobic contacts with PP2Ac and miscellaneous contacts with the B56δ core and B56-IL (III) (Fig. 1b and Extended data Fig. 7c); at the other side, the upper N-arm passes through the cleft between the A-subunit and the B56δ core and makes different modes of contacts with both (IV) (Fig. 1b and Extended data Fig. 7d).

Intriguingly, the N/C-arm crossover is most rich in repulsive contacts (Fig. 1b). Most prominently, E200 in B56-IL makes repulsive contacts to D578 in the C-arm and unfavorable

contacts to several hydrophobic residues in the N/C-arms, I72, Y74, and I582 (Fig. 2a). In addition, E84 in the N-arm makes unfavorable contacts with Y580, a hydrophobic residue in the C-arm (Fig. 2a). These repulsive contacts, together with the energetically unfavorable bending of the N/C-arms, make the crossover the "hottest" hubs along the long dynamic interface. Other unfavorable contacts involve a nearby residue R86 in the upper N-arm (Fig. 2a). The E197K ID mutation creates two repulsive contacts to R571 and K73 in the C-arm and N-arm, respectively (Fig. 2a). Such changes might reduce the number of conformational states of the holoenzyme, and thus allowed us to determine the structure of the closed form of the holoenzyme using single-particle cryo-EM.

We further mapped the hydrophobic contacts along the dynamic interface (Fig. 2b). While many small patches of hydrophobic contacts intertwine with the above unfavorable contacts, the dominant rich hydrophobic contacts are made by the two visible ends of the C-arm. L568 and L569 in the upper C-arm are nestled in a hydrophobic pocket formed by six PP2Ac residues and make close contacts with F416 from the B56δ core (Fig. 2b, upper right). Near the C-arm's terminus, L595 interacts with I303 and H263 at the B56 SLiM-binding pocket, which is buttressed by contacts between F594 to P64/65/67 in the N-arm (Fig. 2b, lower right). The distinct maps of energetically repulsive and favorable hydrophobic contacts likely dictate the complex regulation of the holoenzyme functions.

Dual autoinhibiton of the holoenzyme and roles of the N/C-arms

The PP2A-B56 holoenzymes target specific substrates via the SLiM-binding pocket and the phosphatase active site that are around 30 Å apart (Extended data Fig. 8). Phospho-substrates containing B56 SLiMs bind to the SLiM -binding pocket, which in turn places the nearby

substrate phosphorylation sites close to the PP2A active site. The closed form of the holoenzyme establishes an elegant mechanism of dual autoinhibition, in which E574 and a cis-B56 SLiM (L_{595}TASQE_{600}) in the C-arm make close contacts to the PP2A active site and the B56 SLiM-binding groove (Fig. 3a). E574 in the C-arm mimicks the substrate phosphate and makes extensive H-bond and salt bridge interactions to basic residues at the PP2A active site (Fig. 3b). We hypothesize that autoinhibition of the holoenzyme is established by both N/C-arms. Consistent with this notion, deletion of the C-arm (1-560 or ΔC) in either the WT holoenzyme or the E200K disease variant drastically increases the phosphatase activity, and the truncation of the N-arm (90-602 or ΔN) also increases the phosphatase activity of both holoenzymes (Fig. 3c). While the binding of the cis-B56 SLiM to the SLiM-binding groove mimicks the substrate SLiMs from substrates[19,26], it is also buttressed by the hydrophobic contacts between the upstream F594 with the N-arm (Fig. 3d). Since the holoenzyme is rapidly denatured during isothermal titration calorimetry (ITC), most likely due to the super-dynamic nature of the N/C-arms, we assessed the binding of the GST-tagged substrate SLiMs from CREB and SYT16 to the full-length and truncated holoenzymes using pulldown assay (Fig. 3e). Consistent with the dynamic nature of the N/C-arms, we noticed a significant fluctuation in the experimental results. Therefore, we repeated the experiments 25 times using three batches of materials to learn about the dynamic range of the substrate SLiM-binding. Since the binding of the E200KΔC holoenzyme least fluctuates among repeats, we normalized the results of all repeats against E200KΔC (Fig. 3f). The calculated P-values showed significant differences between truncated and full-length holoenzymes. Intriguingly, while the truncation of the N-arm increases the phosphatase activity (Fig. 3c), it significantly decreases the binding of substrate SLiMs (Fig. 3e-f). Our data suggested that the N/C arms confer coherent suppression at the phosphatase active

site but opposing roles at the substrate SLiM-binding groove. It is likely that the kink on the C-arm stabilized by the N-arm is required for the suppression of the active site but causes structural tension toward the SLiM-binding groove (Fig. 3a). In the absence of the N-arm, the C-arm binds the SLiM-binding groove tighter with a relaxed kink. Its multipartite contacts with the holoenzyme core, particularly hydrophobic contacts, are largely intact (Fig. 2b).

Activation phosphorylation

In addition to the structural modalities for dual autoinhibiton, the N/C-arms are also rich in phosphorylation sites (Fig. 3a). Among these sites, S88, S89, S90, and S573 are the most frequently phosphorylated sites according to the PhosphositePlus database (phosphosite.org). S89, S90, and S573 make extensive H-bond interactions with acidic residues in the holoenzyme core, namely E95 from the scaffold A-subunit, D130 in the B56δ core, and E198 in the B56-IL (Fig. 4a). Phosphorylation at all these sites are expected to create repulsive contacts that would disrupt the closed form and stimulate the loosening of the holoenzyme, leading to its activation. Consistently, phosphorylation of mouse B56δ at S566 (corresponding to S573 of human B56δ) was found to be associated with the activation of the holoenzyme[40]. Using an antibody that we developed to specifically recognize B56δ phosphorylation at S573 (Extended data Fig. 9), we demonstrated a time-dependent increase of pS573 *in vitro* upon co-incubation of PKA and the holoenzyme (Fig. 4b) and in HEK293 cells upon forskolin-induced cAMP/PKA activation (Fig. 4c).

To detect the conformational changes associated with activation phosphorylation, we developed a split NanoBiT B56δ holoenzyme sensor, in which the SmBiT peptide fragment was inserted in the holoenzyme core immediately downstream of the N-arm and the LgBiT fragment was fused

to the C-terminus of the C-arm (Extended data Fig. 10). The two NanoBiT fragments are spatially separated in the closed form. If the N/C-arms loosen upon activation phosphorylation by PKA, the two fragments can interact and form an active NanoBiT enzyme (Extended data Fig. 10). By expressing the WT and E198K mutant holoenzymes bearing this holoenzyme conformation sensor in HEK293T cells, we showed that both holoenzymes gave increased NanoBiT luciferase activity in response to forskolin and rolipram, the combination of an adenine cyclase activator and a PDE4 inhibitor that increases intracellular cAMP levels (Fig. 4d). The responses of both WT and E198K were abolished by S573Q, corroborating the notion that pS573 is essential for holoenzyme activation.

Both our structural observations and biochemical data support a model of holoenzyme activation upon phosphorylation of the N/C-arms (Fig. 4e). Prior to phosphorylation, the holoenzyme prefers a close conformation with crossover interactions of the N/C-arms to establish dual suppression of both the PP2A active site and the B56 SLiM-binding pocket. Upon phosphorylation of the N/C-arms, the repulsive contacts created at the phosphorylation sites drive the N/C-arms from the close conformation to loosen conformations, allowing access to both the phosphatase active site and the B56 SLiM-binding pocket.

Effects of ID mutations on the holoenzyme allosteric network, autoinhibition, and activation phosphorylation

We reasoned that the super-dynamic interface in the PP2A-B56δ holoenzyme forms a coherent allosteric network connecting the activation phosphorylation sites and the structural elements for autoinhibition. Intriguingly, nearly all ID residues found in Jordan Syndrome patients are spreaded throughout this dynamic interface (Fig. 5a). To gain key insights into this allosteric

network, we performed molecular dynamic (MD) simulations for the closed forms of the holoenzymes for WT and two highly recurrent variants, E198K and E200K. Conventional MD simulations showed that terminal residues of the C-arm are the most dynamic portion of the holoenzyme, but the simulation strategy was not successful in sampling the dissociations of the N/C-arms. We thus adopted an enhanced sampling technique: replica exchange with solute tempering-2 (REST2)[49], with the terminal 8 residues of the N/C-arms placed in a "hot region". Twenty independent replicas were run and the reweighted MD conformations were used to compute the allosteric network. Intriguingly, nearly all ID residues and phosphorylation sites on the N/C-arms are located on or in close proximity to the allosteric network of the holoenzyme (Fig. 5b). Either the E198K or the E200K ID mutation alters the residue weights of all ID residues and phosphorylation sites in the allosteric network globally (Fig. 5c-d), underlying a mechanism of ID mutations in perturbing the coherent dual autoinhibition and phosphorylation-induced holoenzyme activation.

Given the super-dynamic nature of the B56δ holoenzyme, we purified up to ten batches of WT and mutant holoenzymes to assess the effects of ID mutations on the holoenzyme function, including substrate SLiM binding and rates of activation phosphorylation. We observed a statistically highly significant increase in substrate SLiM binding by the E198K ID mutations despite the large range of data fluctuation (Fig. 5e). E420K also shows significant effect on the basal substrate SLiM-binding, while the E200K and E197K variants gave mild effects (Fig. 5e). Next, we further assessed time-dependent changes of pS573 upon forskolin-induced cAMP/PKA activation in WT and CRISPR-edited HEK 293 cells bearing homozygotic E198K, heterozygotic E200K, or homozygotic E420K[50]. While the pS573 level of the WT holoenzyme is increased at a stable rate, the phosphorylation rate of the disease variants fluctuate in a large range among all

experimental repeats (Fig.5f). Our data support a notion that the tight coupling of the dynamic interface, the holoenzyme allosteric network, the regulatory structural elements, and ID mutations render the disease mutations to differentially modulate the basal activity and the activation phosphorylation rates of the holoenzyme. These highly intertwined structural and functional connections are expected to be highly sensitive to experimental conditions and cellular signaling contexts.

Effects of B56δ ID mutations on mitosis

B56 SLiMs are predicted in broad signaling proteins involved in different stages of the cell cycle[17]. Building on previous observations of the role of B56δ at the G2/M checkpoint[42] and mitotic exit[43], we examined whether the ID mutations E198K, E200K or E420K (introduced by CRISPR editing) affect mitotic duration and fidelity of HEK293 cells. We used high temporal resolution live-cell imaging to monitor the mitotic progression in HEK293 cells with either WT or mutant B56δ (Fig. 6a). The stages of mitosis were determined using a far-red SiR-DNA dye. The mitotic duration (from nuclear envelope breakdown (NEBD) to anaphase onset) of the WT cells was 67 min, which was similar to E198K cells (66 min). However, both E200K and E420K cells showed significant reduction in mitotic duration (55 and 63 min, respectively). In addition, among the three mutant cells, only E200K cells showed a significantly lower anaphase time compared to the WT cells. The E200K cells seemed to display lower frequency of mitotic errors compared to E198K and E420K, the two most severe forms of the disease variants. The perturbation of mitosis by ID mutations are likely caused by their ability to alter both the basal activity and cell cycle-dependent changes in the phosphorylation of the holoenzyme.

Discussion

Our cryo-EM structures of the PP2A-B56δ holoenzyme, particularly in its close form, reveal distinct mechanisms of the holoenzyme dual latency and its activation in response to phosphorylations. The super-long dynamic regulation interface of the holoenzyme provides a coherent basis for understanding the holoenzyme dual latency and activation and the shared mechanisms of its diverse disease mutations associated with neurological disorders. The complexity of the holoenzyme regulation resides in the unprecedented length of the regulation interface primarily formed by the intrinsically disordered regions rich in regulatory elements. These include multiple phosphorylation sites on both N/C-arms, a cis-B56 SLiM and E574 on the C-arm that establish dual autoinhibition in the closed form, and other signaling sequences on the C-arm, such as nuclear localization signal (NLS) and SH3-binding motif. In addition, the regulation interface is featured by multiple repulsive contacts that underlie the semi-stable, dynamic nature of the interface that is highly responsive to phosphorylations and disease mutations. Furthermore, REST2 MD simulation reveals an allosteric network closely coupled to the regulation interface, reflecting the structural intricacy and coherency underlying complex holoenzyme regulation.

The results of mother nature on Jordan Syndrome patients also corroborate our above notions on the regulation interface in the B56δ holoenzyme. The latter, in turn, provides key insights into the underlying mechanisms of ID-associated disease mutations. Albeit the mutated residues of diverse variants are widely separated spatially, the super-long regulation interface harbors nearly all of them like an extended umbrella. The coupling of ID mutations to the regulation interface and the allosteric network explains why they have a shared list of miscellaneous symptoms of neurological disorders, including intellectual disability, hypotonia, delayed development or loss of verbal skills, autism, etc[8,9,12,13]. ID mutations at the holoenzyme regulation interface might

perturb the holoenzyme regulations and functions in many possible scenarios leading to dominant negative effects. For example, ID mutations might perturb the dual latency individually or simultaneously and alter the activation phosphorylation rates of the holoenzyme. Furthermore, the loss of coherent dual latency and perturbed holoenzyme activation might also lead to untimed exposure of NLS and binding sites for SH3 and 14-3-3. Consistent with the later notion, a family pedigree with B56δ missing the C-arm showed incomplete penetrance of neurological disorders compared to other variants that have heterozygotic single missense mutation[51]. The dominant negative effects of Jordan Syndrome mutations are also supported by studies using CRISPR-edited HEK293 cells bearing heterozygotic or homozygotic B56δ E420K[50]. This mutation in either single or both alleles perturbs the same diversity of signaling nodes, supporting the dominant negative effects of Jordan syndrome mutations.

The involvement of the B56 SLiM and its binding groove at the regulation interface likely contribute to the bulk of the broad range of clinical symptoms of Jordan Syndrome. The human proteome has ~1,500 B56 SLiM-containing proteins involved in broad cellular signaling and processes. Perturbation of the dual latency and phosphorylation-induced holoenzyme activation are expected to affect many of these B56 SLiM-containing signaling proteins. Consistently, CRISPR-edited HEK293 cells bearing B56δ E420K altered 6% of phosphopeptides in the proteome by at least 2-fold[50]. By bioinformatic search, we showed that among ~1,000 genes in SFARI (Simons Foundation Autism Research Initiative) database with mutations that cause neurological disorders (sfari.org), >10% possess B56-targeting SLiMs (data not shown), underlying overlapping molecular processes perturbed by Jordan Syndrome and other mutations that cause neurological disorders. In addition to the effects of ID mutations on mitosis (Fig. 6), the E420K mutation was shown to affect mTOR/AKT signaling among diverse other signaling

processes[50]. Coupling to PP2A holoenzyme SLiMs is a rising theme of signaling and functional complexity. For example, the multiple PP2A holoenzyme SLiMs in PP2A methylesterase (PME-1) creates versatile PME-1 activities toward PP2A holoenzymes and diverse signaling pathways and cellular processes[31].

In addition to the shared mechanisms of its diverse variants, our study began to illuminate the molecular basis that correlates with the clinical severity. Clinical studies showed that E198K is the most severe form of the disease and that E420K is more severe than the E200K and E197K variants[8,9,12]. We showed that the E198K holoenzyme has a much higher basal level of substrate SLiM-binding than the WT holoenzyme and other disease variants (Fig. 5e). Furthermore, E198K and E420K cause longer mitotic duration than WT and E200K, and gave higher mitotic error rates than the E200K variant (Fig. 6). In a companion paper focusing on the changes of the holoenzyme allosteric paths by E198K and E200K, we showed that the E198K holoenzyme has an allosteric path resembling the holoenzyme with activation phosphorylations, underlying a higher basal activity and loss of latency of this variant[52]. In contrast, the allosteric pathway is minimaly affected by E200K. Many questions remain to be answered. Our study laid a critical foundation for understanding the function and regulation of the B56δ holoenzyme and an in-depth understanding of the underlying mechanisms of Jordan Syndrome mutations.

It is important to stress the super-dynamic nature of the regulation interface formed by the disordered N/C-arms and the holoenzyme core. Our challenges to capture the closed form of the WT holoenzyme by single-particle cryo-EM suggests the presence of many conformation states that might be required for numerous nuances of cellular signaling under normal physiological conditions. Two distinct structural features might contribute to the super-dynamic nature: the interactions of two extended intrinsically disordered regions from the widely separated N/C-arms

and the multiple repulsive contacts along the interface. Enriching broad regulation elements in the disordered regions forms one more basis for the complexity and intricacy of this regulation interface. The structural and functional features outlined here might not be unique to the B56δ holoenzyme, but a common theme remains to be uncovered for modulating complex biological processes and signaling.

Author Contributions

CGW performed cryo-EM studies, assisted and guided by HW, BC, and YX. CGW and YX determined the structures. CGW, VKB, and PSP performed biochemical studies, assisted by RS. KK performed REST2 simulation, guided by XH and YX. BEW generated anti-pS573 antibody. MS, AM generated CRISPR cell lines, guided by RH. YCC, CGW and RS performed cell biology, guided by YX and AS. RAM developed and tested the holoenzyme sensor, guided by SS. YX performed data analysis and structural analysis, developed the figure panels, and wrote the manuscript, assisted by CGW.

Acknowledgement

We thank Drs Janette Myers from PNCC (Pacific Northwest Cryo-EM Center) for assistance and discussions on cryo-EM data collection, and Kenneth Satyshur and Ivan Andrewjeski from School of Medicine for IT support. Cryo-EM data collection was supported by NIH grant U24GM129547 and performed at PNCC at OHSU and accessed through EMSL (grid.436923.9), a DOE Office of Science User Facility sponsored by the Office of Biological and Environmental Research. This study is supported by NIGMS R01 GM137090-01 (YX) and Jordan's Guardian Angels Foundation and Jordan's Syndrome research consortium fund from the State of

California A19-3376-5007 (YX, subaward from 2021 SB 129 #44, 2018 SB 840, PD/PI: Nolta, Jan).

Materials and Methods

Protein preparation

All protein constructs were generated by standard PCR molecular cloning strategy. The His_6-tagged scaffold A-subunit, His_8-tagged PP2Ac, and GST-tagged B56δ was overexpressed in insect cells using the lab modified Bac-to-Bac baculovirus expression system[53,54]. Briefly, Hi-5 cells grown to a density of 1.5×10^6 cell/ml were co-infected with PP2A His-Aα, His-Cα and GST-B56δ baculovirus for 48h at 27ºC. Cells were lysed by Dounce homogenization in the lysis buffer containing 25mM Tris-HCl (pH 8.0), 150mM NaCl, 50 μM $MnCl_2$, 2mM DTT and protease inhibitors (10μM leupeptin, 0.5 μM Aprotinin and 1mM PMSF). The insoluble proteins were removed by centrifugation and the soluble fraction of cell lysates was gravity-loaded to GS4B (Glutathione Sepharose 4B) resin (Cytiva) column for three times followed by two washes using 5 column volumes (CV) of lysis buffer. The proteins left on the resins were digested by the TEV protease and the flow-through was further fractionated by anion exchange chromatography (Source 15Q column, Cytiva) and gel filtration chromatography (Superdex 200 column, Cytiva). The point mutations for the B56δ disease variants and/or truncations of the B56δ N/C-arms were introduced by site-directed mutagenesis and the mutant and/or truncated holoenzymes were expressed and purified similar to the WT holoenzyme. GST-tagged SYT16 (132-147) and CREB (99-161) were overexpressed in E. coli DH5α, and purified over GS4B resin and ion exchange chromatography.

GST-mediated pulldown assay

To test the interaction between WT and mutant PP2A-B56δ holoenzyme with substrate B56 SLiMs, 12 μg of GST-tagged SYT16 (132-147) or GST-tagged CREB (99-161) was immobilized on 5 μl of GS4B resin. The unbound protein was washed out by assay buffer containing 25 mM Tris (pH 8.0), 150 mM NaCl, 3 mM DTT and 1x protease inhibitor cocktail (P8340, Sigma). 10 μM of PP2A-B'δ holoenzymes were then added to the immobilized GST-tagged protein in a final volume of 50 μl assay buffer supplemented with 1mg/ml of BSA. After 5 min of incubation, the unbound proteins were removed, and the resins were washed three times by the assay buffer supplemented with 0.1% of Triton X-100 for three times. The proteins remain on the resin were examined by SDS-PAGE and visualized by Coomassie blue staining.

Cross-linking mass spectrometry (XL-MS) of the PP2A-B56δ holoenzyme

The intra-molecular interactions in the PP2A-B56δ holoenzyme was probed by EDC zero-length chemical crosslinker, followed by mass spectrometry analysis. In brief, 1.5 μM PP2A-B56δ holoenzyme in 25 mM MES (pH6.0) and 150mM NaCl was incubated with 60 mM EDC at RT for 75 min, followed by quenching the reaction with 100 mM Tris. The crosslinked samples were desalted by desalting columns (Zepa spin desalting column, Thermo Fisher Scientific) and analyzed by SDS-PAGE. The bands represent holoenzymes with inter-subunit crosslink were excised from SDS-PAGE for reduction and in-gel digestion. The excised bands were reduced in 25mM DTT and 25mM NH_4HCO_3 in 57ºC for 30 min and alkylated with 55mM IAA in 25mM NH_4HCO_3 in darkness for 30min at RT, followed by digestion in 20 μl of 10ng/ul Trypsin (Promega) in 25mM NH4HCO3 (pH 8.0-8.5) and 0.01% ProteaseMAX w/v (Promega) for 16 hr at 37ºC. To improve peptide detection and sequence coverage, secondary digestion was performed with 20ng/μl GluC or chymotrypsin in 25mM NH_4HCO_3 for 8 hr at 37ºC and quenched by 0.05% TFA, followed by desalting with C18 cartridges. The resulting samples were

then separated and analyzed by LC-MS/MS using Lumos mass spectrometer. The identification of peptides for all three subunits was conducted by MeroX software[55]. Multiple XL-MS experiments were performed and four with 90% sequence coverage were used to identify crosslined residue pairs. The detection frequency for reliable residue pairs were evaluated using those in close proximity in the crystal structure of the PP2A-B56γ1 holoenzyme (PDB: 2NPP).

Cryo-EM sample preparation and data acquisition

The cryo-EM grids for the WT PP2A-B56δ holoenzyme was prepared at the New York Structural Biology Center using a prototype of the commercial Chameleon system (SPT Labtech) based on the Spotiton technology[45,46]. 50 pl of the WT holoenzyme at a concentration of 1.6 mg/ ml was applied to the home-made self-wicking nanowire grids[56] using a piezo-electric dispenser, followed by plunge-frozen in liquid ethane. The robot chamber was operated at room temperature without strictly controlled, but moderate, humidity. The cryoEM data for the WT holoenzyme was collected using Titan Krios (ThermoFisher) electron microscope operated at 300 kV equipped with Gatan K2 summit cameras. A total of 1790 movies were automatically acquired by Leginon[57] with a defocus range of -1.2 to -2μm at a nominal magnification of 105,000×, corresponding to a pixel size of 1.096 Å/pixel. Each stack dose-fractioned over 50 frames was recorded with a total exposure time of 9 s and electron dose of 66.84 $eÅ^{-2}$.

For the E197K PP2A-B56δ holoenzyme, an aliquot of 3 μl of purified holoenzyme at 0.4 mg/ml was applied onto a glow-discharged holey gold grids (UltraAuFoil R1.2/1.3), blotted for 4 s with a blot force of -5 and plunge frozen in liquid ethane using a FEI Vitrobot Mark IV (Thermo Fisher Scientific) at 4ºC and 100% humidity. Cryo-EM data was collected using a Titan Krios operating at 300 kV with a Gatan K3 detector and GIF Quantum energy filter. A total of 9158 movies were collected using SerialEM, with a slit width of 20 eV on the energy filter and a

defocus range from -0.7 µm to -2.2 µm in super-resolution counting mode at a nominal magnification of 81,000×, corresponding to a pixel size of 1.068 Å/pixel. Each stack dose-fractioned 69 frames was recorded for a total of exposure time of 3.2 s and electron dose of 49 e-/Å^2.

Cryo-EM data processing

All data were processed with similar strategies and procedures using cryoSPARC 2.0[58]. Movies were motion-corrected using Patch Motion Correction, followed by the contrast transfer function (CTF) estimation using Patch CTF Estimation. Images with bad CTF estimations (>4 Å) were discarded. Particles were first picked from thirty good images using Blob Picker and extracted with a box size of 280Å. Good 2D class averages showing projections in different orientations were selected as templates for automatic picking for the entire dataset. Reiterate 2D classification was used to remove bad particles. The remaining good particles were used for ab initio reconstruction, followed by heterogeneous and homogenous refinement, with particles from bad classes removed in each reiterate procedure. Different conformations of the PP2A-B56δ holoenzyme were best separated by 3D variability analysis (3DVA)[59]. Particles from conformationally homogeneous classes were then subjected to homogenous refinement, followed by local and global CTF refinement. Local refinement with a mask around the close conformation of the B56δ subunit was performed to obtain a better overall resolution for this subunit. These efforts gave maps with a resolution of 3.13 Å for the loose form and 2.59 Å for the closed form of the E197K PP2A-B56δ holoenzyme. The resolution was estimated by applying a soft mask around the protein complex and using the gold-standard Fourier shell correlation (FSC) = 0.143 criterion.

Model building and refinement

The initial model of the PP2A-B56δ complex was built on the structure of PP2A-B56γ1 holoenzyme (PDB ID: 2NPP) and manually docked into the cryo-EM maps in Chimera[60]. Modifications to the holoenzyme core and model building of the N/C-arms were performed in COOT[61]. The structural model was refined using the phenix.real_space_refine program in PHENIX[62] with secondary structure and geometry restraints. Model was analyzed using MolProbity[63].

Phosphatase assay

The enzyme kinetics of the purified PP2A-B56δ holoenzymes were determined using the PiColorLock phosphatase assay (Abcam, Ab270004) measuring the release of inorganic phosphate from the dephosphorylation of substrates. A phosphorylated hexapeptide (KRpTIRR) was used as the substrate for the assay. 50ul of 30nM indicated PP2A-B56δ holoenzymes in the assay buffer, containing 25mM Tris pH8.0, 150mM NaCl, and 50uM $MnCl_2$ supplemented with 0.05 mg/ml BSA, were added to the 10µl substrate (6 times of the final concentration prepared in the assay buffer) in a 96-well clear plate to start the reactions. After 3 min, the reactions were quenched by 15 µl of quench buffer provided in the kit and allowed the color to develop for 15 min. The absorbance at 635nm of the reactions was then read by the SpectraMax Plus 384 Microplate Reader (Molecular Devices) using the end-point mode. Initial velocity (V_0) determined at varying concentrations of substrate was calculated and fit to the Michaelis–Menten equation (eq. 1) to determine the steady-state kinetics of the PP2A-B56 holoenzymes.

$$v = \frac{k_{cat}[E][S]}{K_m + [S]} \quad (1)$$

In eq. 1, kcat is the rate constant, [E] and [S] are the enzyme and substrate concentration, and Km is the Michaelis-Menten constant reflecting the binding affinity between the peptide substrate and the enzyme.

In vitro holoenzyme phosphorylation by protein kinase A (PKA)

100 µl PP2A-B56δ holoenzyme was prepared to a final concentration at 0.1mg/ml in assay buffer containing 50 mM Tris-HCl (pH7.5), 10 mM $MgCl_2$, 200 uM ATP, 0.1 mM EDTA, 2 mM DDT and 0.01% Brij35. Phosphorylation was initiated by adding 1 µl PKA at 0.1mg/ml to the PP2A-B56δ holoenzymes (PKA: PP2A-B56δ = 1: 100 (w/w)) and incubating the mixture at 37°C. 10 µl PP2A-B56 holoenzyme was taken out at indicated time from the reaction, mixed with 3 µl of 4x SDS dye (40% Glycerol, 8% SDS, 0.25M Tris-HCL, pH 6.8,0.4M DTT,0.04% bromophenol blue) and immediately heated at 95°C for 3 min to quench the reaction. 0.05 µg of PP2A-B56 holoenzyme from each time point were examined by western blot using the antibody that specifically recognizes phosphorylation of S573 of PP2A-B56δ holoenzyme.

REST2 simulation

The cryo-EM structure of the closed form of the E197K PP2A-B56δ holoenzyme was used to generate the initial model for the close froms of WT, E198K, and E200K holoenzymes. Molecular dynamics (MD) simulations were performed using Gromacs[64] patched with PLUMED 2.8.0 in the Amber ff14SB forcefield[65]. The protonation state of protein residues was determined by propka 3.4.0. The short-range coulomb interactions were cut off at 0.9 nm and long-range electrostatics were computed with PME. The Lennard-Jones interactions were cut off at 0.9 nm. The structure was simulated in a dodecahedron box, with the minimum distance to the surface of the protein of 1 nm. The complex was solvated in TIP3P water (approximately 60,000

water molecules) and sodium ions were added until the system was neutral (31 ions for the WT complex and 29 for the E198K and E200K variants). The energy of the system was minimized with the steepest descent algorithm for 10,000 steps. Then, 1 ns MD simulations were performed at 310K with the positions of all protein atoms except hydrogen restrained. In these simulations temperature was controlled by a V-rescale thermostat with a coupling constant of 10 ps, and pressure set to 1 bar controlled by a C-rescale barostat with a coupling constant of 1 ps.

Conventional MD simulations are not successful in sampling the dissociations of the N/C-arms. We thus have adopted an enhanced sampling technique: REST2[49], with the terminal 8 residues of the N/C-arms placed in a "hot region". 20 independent replicas were run with the potential of the "hot region" scaled to temperatures from 310K to 600K. The MD conformations were then reweighted to the canonical ensemble at 310K using RE-SWHAM[66] to obtain structural and thermodynamic properties, and to compute the allosteric network using an established method[67]. The weight of each residue in the network was computed as the normalized number of all shortest paths in the network crossing its vertex.

Mammalian cell holoenzyme sensor to detect conformation transition upon activation

N-terminal large (LgBit) and C-terminal small (SmBit) fragments derived from NanoLuc (Promega, Madison, WI, USA) were fused to the C-terminus of B56δ and inserted downstream of its N-arm at residue 103, respectively. The SmBit sequence is sandwiched by a short linker sequence, "GSG" at both ends to alleviate structural hindrance for complementation with LgBit. The constructs expressing the B56δ holoenzyme conformation sensors were transfected into Cos1 cells. After 24 hours, cells were placed in 20% Nano-Glo® Live Cell Reagent (Promega) mixed with 80% DMEM containing 1% FBS. Cells were equilibrated at 37 °C in 5% CO_2 in a Cytation 5 before the luminescence readings were measured every 5 minutes. Following the second reading,

cells were treated with 20 μM forskolin (Tocris) and 2 μM rolipram (Tocris) to activate adenylyl cyclase and inhibit cAMP phosphodiesterase 4 (PDE4) simultaneously to activate cellular cAMP/PKA. All values were normalized to vehicle treated control wells and every well was normalized to its 5-min time point (just prior to forskolin/rolipram treatment). The experiments were performed in quadruplicate and repeated three times. Representative results were shown. Error bars represent standard deviation.

Mammalian cell culture and the time-course of B56δ phosphorylation upon cellular cAMP activation

Human embryonic kidney cells (HEK293T) cells were cultured in Dulbecco's modified Eagle's medium (Gibco, Thermo Fisher Scientific, Waltham, MA, USA) with 10% fetal bovine serum (Hyclone, GE Healthcare, Boston, MA, USA), 100 U/ml penicillin, and 100 μg/ml streptomycin in a humidified atmosphere at 37 °C with 5% CO2.

Following transit transfection of the Flag-tagged B56δ (WT, E198K, E200K and E420K), the HEK293T cells were treated with 10uM forskolin (Fsk; Sigma: 344270-10MG) and 1mM isobutylmethyxanthine (IBMX; Cayman:13347) to stimulate cellular cAMP/PKA. The cells were harvested at indicated time following stimulation and lysed using buffer containing 20mM Tris-HCl pH7.0, 150mM NaCl, 0.1% Triton X-100, 10uM H89 (PKA inhibitor), 10ug/ml DNase, protease inhibitor and phosphatase inhibitor (phoSTOP, Sigma-Millipore). Total cell lysates (20 μg) for each timepoint were examined by Western analysis. To detect the level of phosphorylation at S573 of B56δ, we utilized a newly developed antibody that recognizes the phospho-S573 (pS573). The levels of pS573 were normalized to total B56δ detected by the specific antibody (Invitrogen-Thermal Scientific, MA-26636). At least five experimental repeats

were performed to determine the fluctuation range of the activation phosphorylation rates. The P-values for the time-dependent increase of pS573 were calculated using Jonckheere-Terpstra test in MSTAT7.0 (https://oncology.wisc.edu/mstat/).

CRISPR knockin of B56δ ID mutations

The CRISPR knockin of the E198K and E200K B56δ single mutations were carried out similarly to the knockin of E420K as previously described[50]. Briefly, BE4-Gam, a fourth-generation genomic base editor, was used to create stable HEK- 293 cell lines containing homogenous E420K, E198K, and heterogenous E200K. Well-positioned endogenous PAM sequences in PPP2R5D facilitated base editing. The gRNAs positioned the cytidine deaminase precisely over the targets while simultaneously positioning the nCas9 to nick the DNA strand containing the unedited guanine to facilitate mismatch repair mechanisms. The correct base editing was enhanced by the fusion of inhibitors of base excision repair. Cells were sorted 48 h after transfection to allow time for replication, after which the base edit becomes a permanent change in the genome. By Sanger sequencing, we confirmed the genotype of cell lines containing the desired variants. To ensure the cell lines were homogeneous, each clonal-derived line was single-cell sorted three times before further analysis. Complete genomic sequencing of the parental and variant cell lines was performed to characterize the genomic background, detect any off-target editing, and ensure that the repetitive single-cell sorting did not introduce spontaneous somatic mutations. Cell lines with off-target or random mutations in protein-coding regions were discarded. Detailed descriptions of the above CRISPR-edited cell lines will be described elsewhere.

Live cell imaging and mitotic duration measurements

To investigate whether the B56δ ID mutation, E198K, E200K or E420K affects mitotic duration and fidelity, we used high temporal resolution live-cell imaging to monitor the mitotic progression of HEK293T cells with the WT B56δ or CRISPR knockin ID mutation. Nikon Ti-E inverted microscope equipped with a Photometrics CoolSnap Hq2 CCD camera, spectra-X LED light source (Lumencor), and a Plan Apo 20x objective (NA = 0.45) controlled by Nikon Element software was used for live imaging. Time-lapse imaging collected 5 frame 3D stacks at 2 μm steps along the z-axis at 3 min intervals for 24-48 hours. All cells were grown on a 4-chambered glass bottom dish (#1.5 glass, Cellvis) in FluoroBrite DMEM media (Thermo Fisher) supplemented 10% FBS (Gibco) and 2 mM GlutaMAX (Gibco). All cells were incubated with sirDNA and 10 μM of verapamil (Cytoskeleton, Inc.) for 4 hours prior to start live imaging. Cells were recorded at 37°C with 5% CO2 in a stage-top incubator using the feedback control to stably maintain the growing media's temperature (Tokai Hit, STX model). Image analysis was performed using Nikon Element software. Mitotic stages were determined by nuclear staining. The mitotic duration was measured from nuclear envelope breakdown (NEBD) to anaphase onset. Incidences of lagging chromosomes were anlyzed. The experiments were independently repeated three times and P-values between variants were calculated by One-Way Anova and two-tailed t-test. P-values < 0.05 were considered as significant.

References

1. Arnold, H.K. & Sears, R.C. A tumor suppressor role for PP2A-B56α through negative regulation of c-Myc and other key oncoproteins. *Cancer and Metastasis Reviews* **27**, 147-158 (2008).
2. Wlodarchak, N. & Xing, Y. PP2A as a master regulator of the cell cycle. *Crit Rev Biochem Mol Biol* **51**, 162-84 (2016).
3. Virshup, D.M. Protein phosphatase 2A: a panoply of enzymes. *Curr Opin Cell Biol* **12**, 180-5 (2000).
4. Strack, S. et al. Protein phosphatase 2A holoenzyme assembly: identification of contacts between B-family regulatory and scaffolding A subunits. *J Biol Chem* **277**, 20750-5 (2002).
5. Saraf, A., Oberg, E.A. & Strack, S. Molecular determinants for PP2A substrate specificity: charged residues mediate dephosphorylation of tyrosine hydroxylase by the PP2A/B′ regulatory subunit. *Biochemistry* **49**, 986-995 (2010).
6. Shi, Y. Serine/threonine phosphatases: mechanism through structure. *Cell* **139**, 468-84 (2009).
7. Study., D.D.D. Prevalence and architecture of de novo mutations in developmental disorders. *Nature* **542**, 433-438 (2017).
8. Shang, L. et al. De novo missense variants in PPP2R5D are associated with intellectual disability, macrocephaly, hypotonia, and autism. *Neurogenetics* **17**, 43-9 (2016).
9. Houge, G. et al. B56delta-related protein phosphatase 2A dysfunction identified in patients with intellectual disability. *J Clin Invest* **125**, 3051-62 (2015).
10. Cerami, E. et al. The cBio cancer genomics portal: an open platform for exploring multidimensional cancer genomics data. *Cancer Discov* **2**, 401-4 (2012).
11. Gao, J. et al. Integrative analysis of complex cancer genomics and clinical profiles using the cBioPortal. *Sci Signal* **6**, pl1 (2013).
12. Biswas, D., Cary, W. & Nolta, J.A. PPP2R5D-Related Intellectual Disability and Neurodevelopmental Delay: A Review of the Current Understanding of the Genetics and Biochemical Basis of the Disorder. *Int J Mol Sci* **21**(2020).
13. Oyama, N. et al. Clinical, neuroimaging and molecular characteristics of PPP2R5D-related neurodevelopmental disorders: an expanded series with functional characterisation and genotype-phenotype analysis. *J Med Genet* (2022).
14. Walker, I.M. et al. PPP2R5D Genetic Mutations and Early-Onset Parkinsonism. *Ann Neurol* **89**, 194-195 (2021).
15. Hetzelt, K. et al. Early-onset parkinsonism in PPP2R5D-related neurodevelopmental disorder. *Eur J Med Genet* **64**, 104123 (2021).
16. Kim, C.Y. et al. Early-Onset Parkinsonism Is a Manifestation of the PPP2R5D p.E200K Mutation. *Ann Neurol* **88**, 1028-1033 (2020).
17. Wu, C.G. et al. PP2A-B' holoenzyme substrate recognition, regulation and role in

cytokinesis. *Cell Discov* **3**, 17027 (2017).
18. Hertz, E.P. et al. A Conserved Motif Provides Binding Specificity to the PP2A-B56 Phosphatase. *Mol Cell* **63**, 686-95 (2016).
19. Wang, J. et al. Crystal structure of a PP2A B56-BubR1 complex and its implications for PP2A substrate recruitment and localization. *Protein & cell* **7**, 516-526 (2016).
20. Davey, N.E. & Morgan, D.O. Building a regulatory network with short linear sequence motifs: lessons from the degrons of the anaphase-promoting complex. *Molecular cell* **64**, 12-23 (2016).
21. Davey, N.E., Cyert, M.S. & Moses, A.M. Short linear motifs–ex nihilo evolution of protein regulation. *Cell Communication and Signaling* **13**, 43 (2015).
22. Wigington, C.P. et al. Systematic discovery of Short Linear Motifs decodes calcineurin phosphatase signaling. *Molecular Cell* **79**, 342-358. e12 (2020).
23. Ueki, Y. et al. A consensus binding motif for the PP4 protein phosphatase. *Molecular Cell* **76**, 953-964. e6 (2019).
24. Heroes, E. et al. The PP1 binding code: a molecular-lego strategy that governs specificity. *The FEBS journal* **280**, 584-595 (2013).
25. Nasa, I., Rusin, S.F., Kettenbach, A.N. & Moorhead, G.B. Aurora B opposes PP1 function in mitosis by phosphorylating the conserved PP1-binding RVxF motif in PP1 regulatory proteins. *Science signaling* **11**(2018).
26. Wang, X., Bajaj, R., Bollen, M., Peti, W. & Page, R. Expanding the PP2A Interactome by Defining a B56-Specific SLiM. *Structure* **24**, 2174-2181 (2016).
27. Kruse, T. et al. Direct binding between BubR1 and B56-PP2A phosphatase complexes regulate mitotic progression. *J Cell Sci* **126**, 1086-92 (2013).
28. Bastos, R.N., Cundell, M.J. & Barr, F.A. KIF4A and PP2A-B56 form a spatially restricted feedback loop opposing Aurora B at the anaphase central spindle. *J Cell Biol* **207**, 683-93 (2014).
29. Ueki, Y. et al. A highly conserved pocket on PP2A-B56 is required for hSgo1 binding and cohesion protection during mitosis. *EMBO Rep* **22**, e52295 (2021).
30. Ito, A. et al. A truncated isoform of the PP2A B56 subunit promotes cell motility through paxillin phosphorylation. *Embo J* **19**, 562-71 (2000).
31. Li, Y. et al. Coupling to short linear motifs creates versatile PME-1 activities in PP2A holoenzyme demethylation and inhibition. *Elife* **11**(2022).
32. Ambjorn, S.M. et al. A complex of BRCA2 and PP2A-B56 is required for DNA repair by homologous recombination. *Nat Commun* **12**, 5748 (2021).
33. Kim, S.H., Wu, C.G., Jia, W., Xing, Y. & Tibbetts, R.S. Roles of constitutive and signal-dependent protein phosphatase 2A docking motifs in burst attenuation of the cyclic AMP response element-binding protein. *J Biol Chem* **297**, 100908 (2021).
34. Lambrecht, C. et al. Loss of protein phosphatase 2A regulatory subunit B56delta promotes spontaneous tumorigenesis in vivo. *Oncogene* **37**, 544-552 (2018).

35. Liu, L. & Eisenman, R.N. Regulation of c-Myc Protein Abundance by a Protein Phosphatase 2A-Glycogen Synthase Kinase 3beta-Negative Feedback Pathway. *Genes Cancer* **3**, 23-36 (2012).
36. Arnold, H.K. et al. The Axin1 scaffold protein promotes formation of a degradation complex for c-Myc. *Embo J* **28**, 500-12 (2009).
37. Arnold, H.K. & Sears, R.C. A tumor suppressor role for PP2A-B56alpha through negative regulation of c-Myc and other key oncoproteins. *Cancer Metastasis Rev* **27**, 147-58 (2008).
38. Arnold, H.K. & Sears, R.C. Protein phosphatase 2A regulatory subunit B56alpha associates with c-myc and negatively regulates c-myc accumulation. *Mol Cell Biol* **26**, 2832-44 (2006).
39. Dodge-Kafka, K.L. et al. cAMP-stimulated protein phosphatase 2A activity associated with muscle A kinase-anchoring protein (mAKAP) signaling complexes inhibits the phosphorylation and activity of the cAMP-specific phosphodiesterase PDE4D3. *J Biol Chem* **285**, 11078-86 (2010).
40. Ahn, J.H. et al. Protein kinase A activates protein phosphatase 2A by phosphorylation of the B56delta subunit. *Proc Natl Acad Sci U S A* **104**, 2979-84 (2007).
41. Flynn, M.P. et al. Luteinizing hormone receptor activation in ovarian granulosa cells promotes protein kinase A-dependent dephosphorylation of microtubule-associated protein 2D. *Mol Endocrinol* **22**, 1695-710 (2008).
42. Margolis, S.S. et al. Role for the PP2A/B56delta phosphatase in regulating 14-3-3 release from Cdc25 to control mitosis. *Cell* **127**, 759-73 (2006).
43. Forester, C.M., Maddox, J., Louis, J.V., Goris, J. & Virshup, D.M. Control of mitotic exit by PP2A regulation of Cdc25C and Cdk1. *Proc Natl Acad Sci U S A* **104**, 19867-72 (2007).
44. Shouse, G.P., Nobumori, Y., Panowicz, M.J. & Liu, X. ATM-mediated phosphorylation activates the tumor-suppressive function of B56gamma-PP2A. *Oncogene* **30**, 3755-65 (2011).
45. Levitz, T.S., Brignole, E.J., Fong, I., Darrow, M.C. & Drennan, C.L. Effects of chameleon dispense-to-plunge speed on particle concentration, complex formation, and final resolution: A case study using the Neisseria gonorrhoeae ribonucleotide reductase inactive complex. *J Struct Biol* **214**, 107825 (2022).
46. Jain, T., Sheehan, P., Crum, J., Carragher, B. & Potter, C.S. Spotiton: a prototype for an integrated inkjet dispense and vitrification system for cryo-TEM. *J Struct Biol* **179**, 68-75 (2012).
47. Xu, Y. et al. Structure of the protein phosphatase 2A holoenzyme. *Cell* **127**, 1239-51 (2006).
48. Cho, U.S. & Xu, W. Crystal structure of a protein phosphatase 2A heterotrimeric holoenzyme. *Nature* **445**, 53-7 (2007).

49. Wang, L., Friesner, R.A. & Berne, B.J. Replica exchange with solute scaling: a more efficient version of replica exchange with solute tempering (REST2). *J Phys Chem B* **115**, 9431-8 (2011).
50. Papke, C.M. et al. A disorder-related variant (E420K) of a PP2A-regulatory subunit (PPP2R5D) causes constitutively active AKT-mTOR signaling and uncoordinated cell growth. *J Biol Chem* **296**, 100313 (2021).
51. Liu, R. et al. A novel nonsense mutation in PPP2R5D is associated with neurodevelopmental disorders and shows incomplete penetrance in a Chinese pedigree. *Clin Neurol Neurosurg* **223**, 107524 (2022).
52. Disease Mutations and Phosphorylation Alter the Allosteric Pathways Involved in Autoinhibition of Protein Phosphatase 2A. (2023).
53. Stanevich, V. et al. The Structural Basis for Tight Control of PP2A Methylation and Function by LCMT-1. *Mol Cell* **41**, 331-42 (2011).
54. Zhang, L. et al. Eya3 partners with PP2A to induce c-Myc stabilization and tumor progression. *Nat Commun.* **9**, 1047. doi: 10.1038/s41467-018-03327-4. (2018).
55. Iacobucci, C. et al. A cross-linking/mass spectrometry workflow based on MS-cleavable cross-linkers and the MeroX software for studying protein structures and protein-protein interactions. *Nat Protoc* **13**, 2864-2889 (2018).
56. Wei, H. et al. Optimizing "self-wicking" nanowire grids. *J Struct Biol* **202**, 170-174 (2018).
57. Suloway, C. et al. Automated molecular microscopy: the new Leginon system. *J Struct Biol* **151**, 41-60 (2005).
58. Punjani, A., Rubinstein, J.L., Fleet, D.J. & Brubaker, M.A. cryoSPARC: algorithms for rapid unsupervised cryo-EM structure determination. *Nat Methods* **14**, 290-296 (2017).
59. Punjani, A. & Fleet, D.J. 3D variability analysis: Resolving continuous flexibility and discrete heterogeneity from single particle cryo-EM. *J Struct Biol* **213**, 107702 (2021).
60. Pettersen, E.F. et al. UCSF Chimera--a visualization system for exploratory research and analysis. *J Comput Chem* **25**, 1605-12 (2004).
61. Emsley, P., Lohkamp, B., Scott, W.G. & Cowtan, K. Features and development of Coot. *Acta Crystallographica Section D: Biological Crystallography* **66**, 486-501 (2010).
62. Adams, P.D. et al. PHENIX: a comprehensive Python-based system for macromolecular structure solution. *Acta Crystallographica Section D: Biological Crystallography* **66**, 213-221 (2010).
63. Chen, V.B. et al. MolProbity: all-atom structure validation for macromolecular crystallography. *Acta Crystallographica Section D: Biological Crystallography* **66**, 12-21 (2010).
64. Hess, B., Kutzner, C., van der Spoel, D. & Lindahl, E. Gromacs 4: algorithms for highly efficient, load-balanced, and scalable molecular simulation. *J. Chem. Theory Comput.* **4**,

435-447 (2008).
65. Maier, J.A. et al. ff14SB: Improving the Accuracy of Protein Side Chain and Backbone Parameters from ff99SB. *J Chem Theory Comput* **11**, 3696-713 (2015).
66. Zhang, B.W., Xia, J., Tan, Z. & Levy, R.M. A Stochastic Solution to the Unbinned WHAM Equations. *J Phys Chem Lett* **6**, 3834-40 (2015).
67. Botello-Smith, W.M. & Luo, Y. Robust Determination of Protein Allosteric Signaling Pathways. *J Chem Theory Comput* **15**, 2116-2126 (2019).

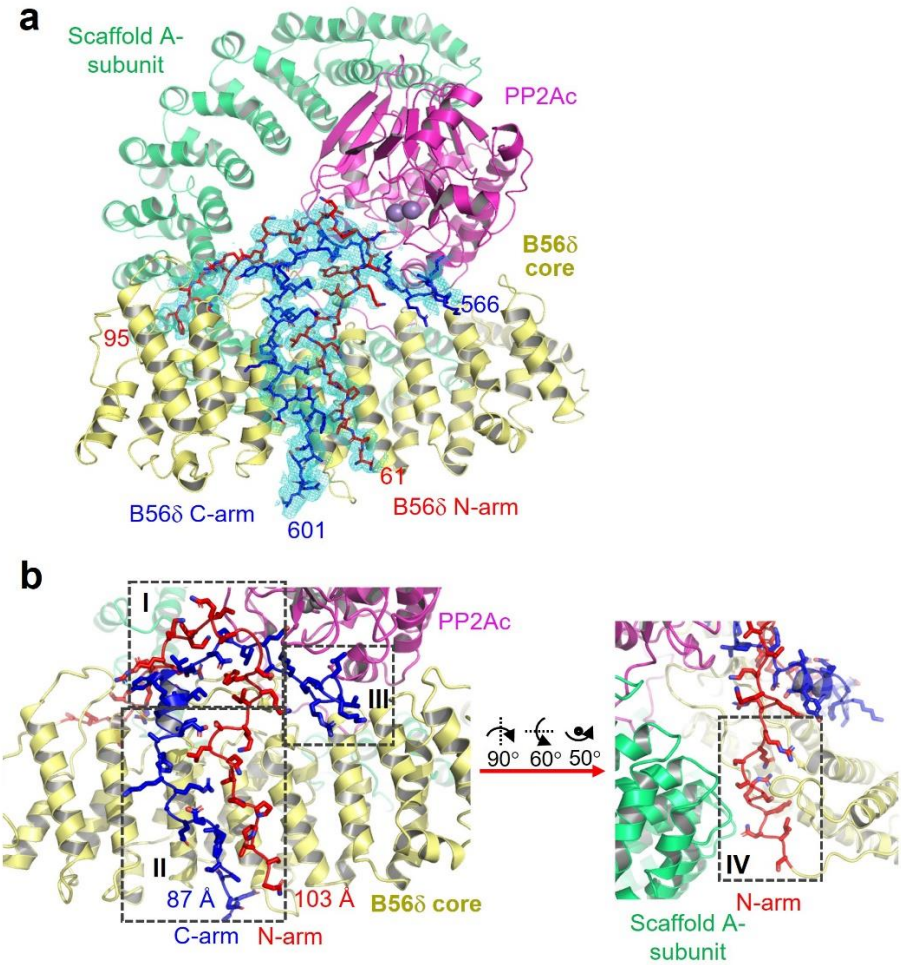

I: N/C-arm crossover-PP2Ac-B56-IL

	N/C	N-PP2Ac	C-PP2Ac	N-IL	C-IL
H-bonds	8	2	4	2	2
Hydrophobic	1	1			
salt bridge					1
unfavorable	1			2	2

II: N/C-arm-B56 core

	N/C	N-Core	C-Core-IL
H-bonds	3	4	8
Hydrophobic	5	2	5
salt bridge			
unfavorable			1

III: C-arm-PP2Ac-B56 core & IL

	C-PP2Ac	C-Core	C-IL
H-bonds		1	2
Hydrophobic	5	1	
salt bridge		1	1
unfavorable			

IV: N-arm-A-subunit-B56 core

	N-A	N-Core
H-bonds	3	8
Hydrophobic		3
salt bridge		1
unfavorable		2

Figure 1. The cryo-EM structure of the closed form of the E197K PP2A-B56δ holoenzyme. (a) The overall cryo-EM structure of the E197K holoenzyme in the closed form. The A subunit, PP2Ac, B56δ core, and N/C-arms are colored green, magenta, yellow, red, and blue, respectively. The electron density map for N/C-arms is colored cyan. The N/C-arms are in sticks and the rest of the structure is in cartoon. (b) Mapping of the contact properties along the path of the super-dynamic interface spanning over 190 Å. The presentation of the structural model and the color scheme are the same as in (a).

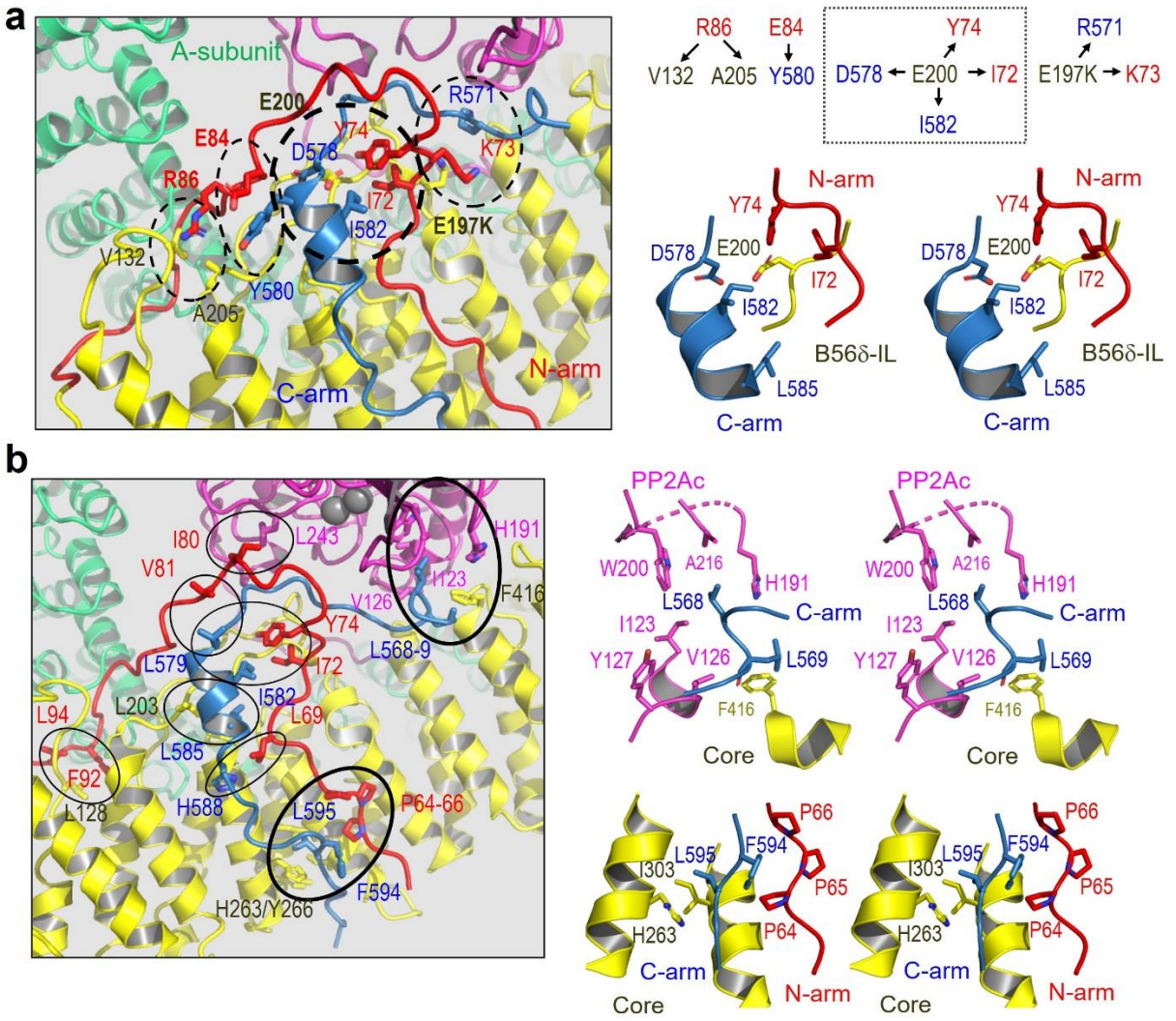

Figure 2. Mapping and closeup views of unfavoarable and hydrophobic contacts along the dynamic interface. (a) Distribution of unfavoarable and repulsive contacts at the dynamic interface, highlighted in hidashed cycles (left) and illustrated at the upper right panel. The closeup stereoview of the central repulsive contacts with E200 is shown at the lower right panel. (b) Patches of hydrophobic contacts are in cycles and major hydrophobic interfaces are highlighted thick cycles (left). The closeup stereoviews for the latter are shown (right). For (a-b), the color scheme is the same as in Fig.1. The structural models are shown in cartoon and key residues at the interfaces are shown in stick.

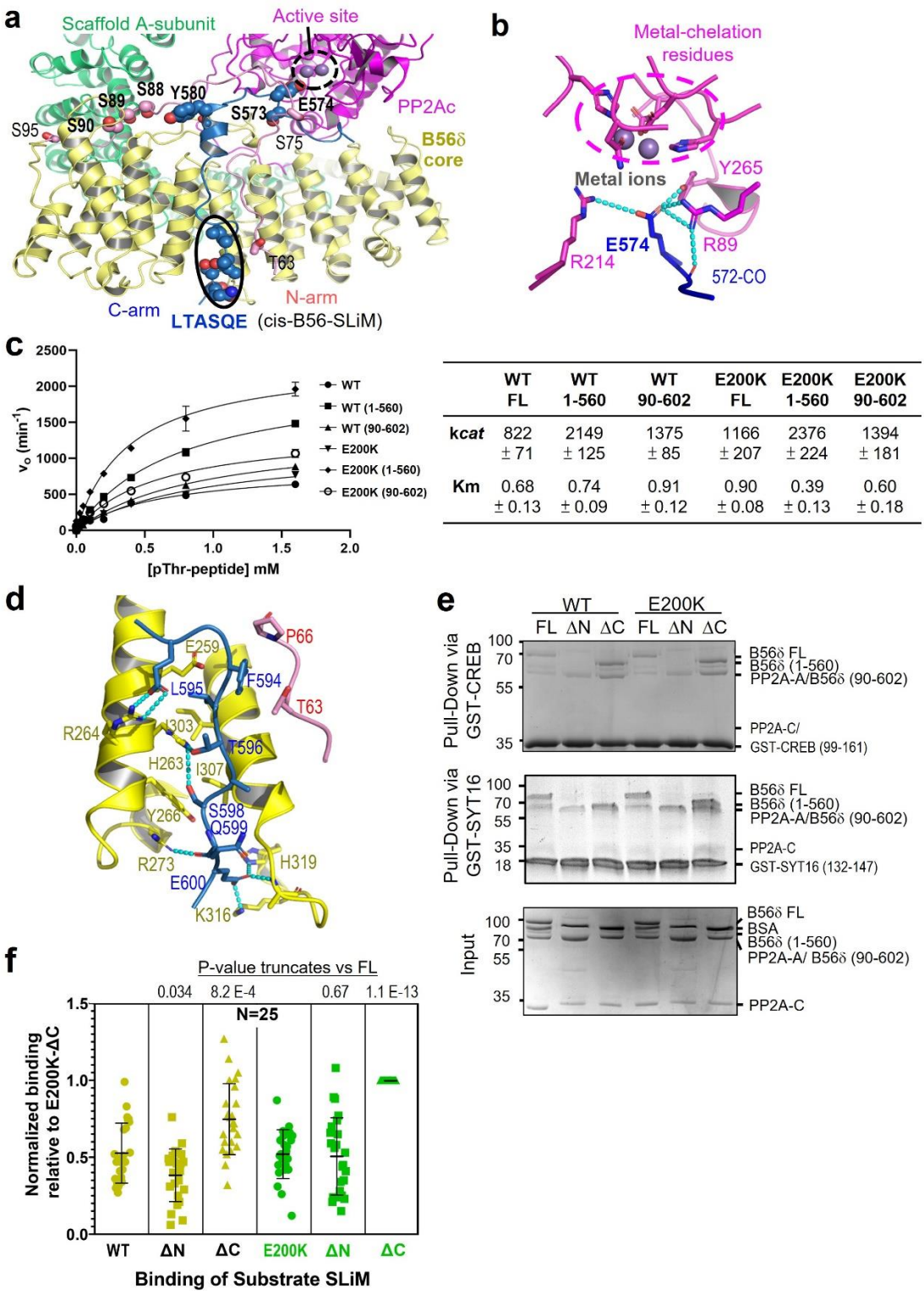

	WT FL	WT 1-560	WT 90-602	E200K FL	E200K 1-560	E200K 90-602
kcat	822 ± 71	2149 ± 125	1375 ± 85	1166 ± 207	2376 ± 224	1394 ± 181
Km	0.68 ± 0.13	0.74 ± 0.09	0.91 ± 0.12	0.90 ± 0.08	0.39 ± 0.13	0.60 ± 0.18

Figure 3. Structural mechanism of dual auto-inhibiton and roles of the B56δ N/C-arms. (a) Overall structure of the PP2A-B56δ holoenzyme highlighting residues on the N/C-arms important for activation phosphorylation and suppression of the phosphatase active site and the SLiM-binding groove. The structure is shown in cartoon and colored as in Fig. 1, except that the

N/C-arms are colored pink and blue, respectively. Residues with key regulation functions are shown in spheres. (b) The closeup view of auto-inhibiton at the phosphatase active site. The active site metal ions are in spheres. Active site residues and E574 from the C-arm are shown in stick. (c) Truncations of either N- or C-arm increase the phosphatase activity of both the WT and E200K holoenzymes. (d) The closeup view of auto-inhibiton at the B56 SLiM-binding groove, buttressed by extended interactions. (e) Examples of pulldown assays of the WT and E200K PP2A-B56δ holoenzyme full length (FL), truncation of N-arm (ΔN) or C-arm (ΔC) via GST-tagged CREB (99-161) (upper) or GST-SYT16 (132-147) (middle). One fifth of the holoenzyme input is shown (lower). (f) All experimental repeats from (e) are normalized to E200KΔC, and the scatter plots of the normalized results, averages of all repeats, and standard error (SEM) are shown. The P-values for the full-length versus truncated holoenzymes are calculated using two-sided Wilcoxon Rank Sum test. For (b) and (d), the structural models are shown in cartoon, and the color scheme is the same as in (a). Residues at the interfaces are shown in stick. H-bond interactions are shown in cyan dashed lines.

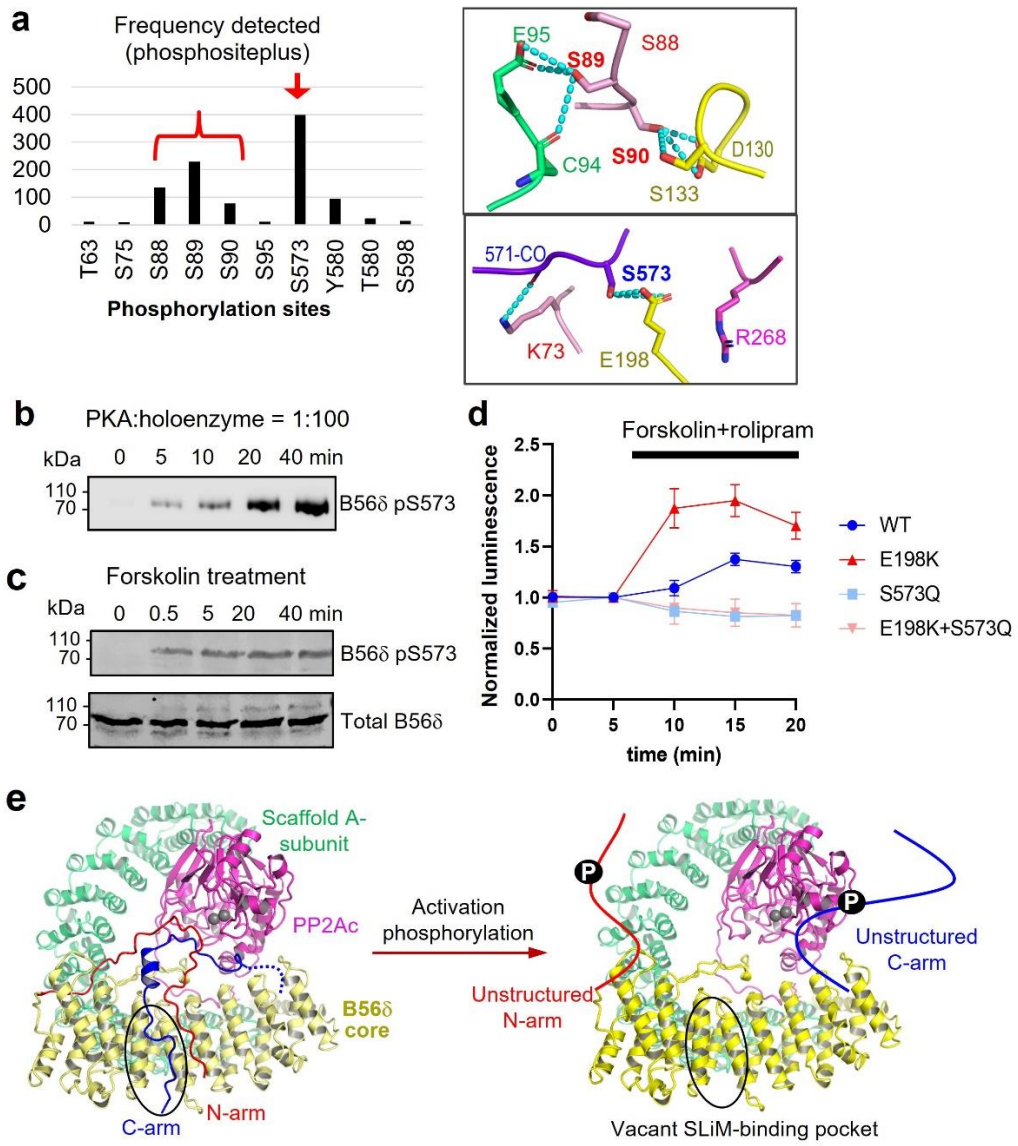

Figure 4. Structural mechanisms of activation phosphorylation of the PP2A-B56δ holoenzyme. (a) The most frequently detected phosphorylation sites on the N/C-arms are highlighted (as summarized from phosphosite.org) (left). The closeup views of these serine residues on the N/C-arms and their interactions at the dynamic regulation interface (right). The color scheme is the same as in Fig. 3a. Phosphorylation at these sites are expected to create repulsive contacts. (b) Time-dependent increase of pS573 of the PP2A-B56δ holoenzyme by PKA *in vitro*. (c) Time-dependent increase of B56δ pS573 upon cellular activation of cAMP/PKA. (d) Time-dependent increase of substrate B56 SLiM binding the PP2A-B56δ holoenzyme (WT and E198K) in mammalian cells upon cellular activation of cAMP/PKA by forskolin and rolipram. The nonphosphorylatable mutation of B56δ, S573Q, abolishes this response. (e) Structural illustration of phosphorylation-induced loosening of the N/C-arms for holoenzyme activation. Phosphorylation of N/C-arms disrupts their interactions with the holoenzyme core, resulting in dual activation of the phosphatase active site and the B56 SLiM-binding groove. The color scheme is the same as in Fig. 1.

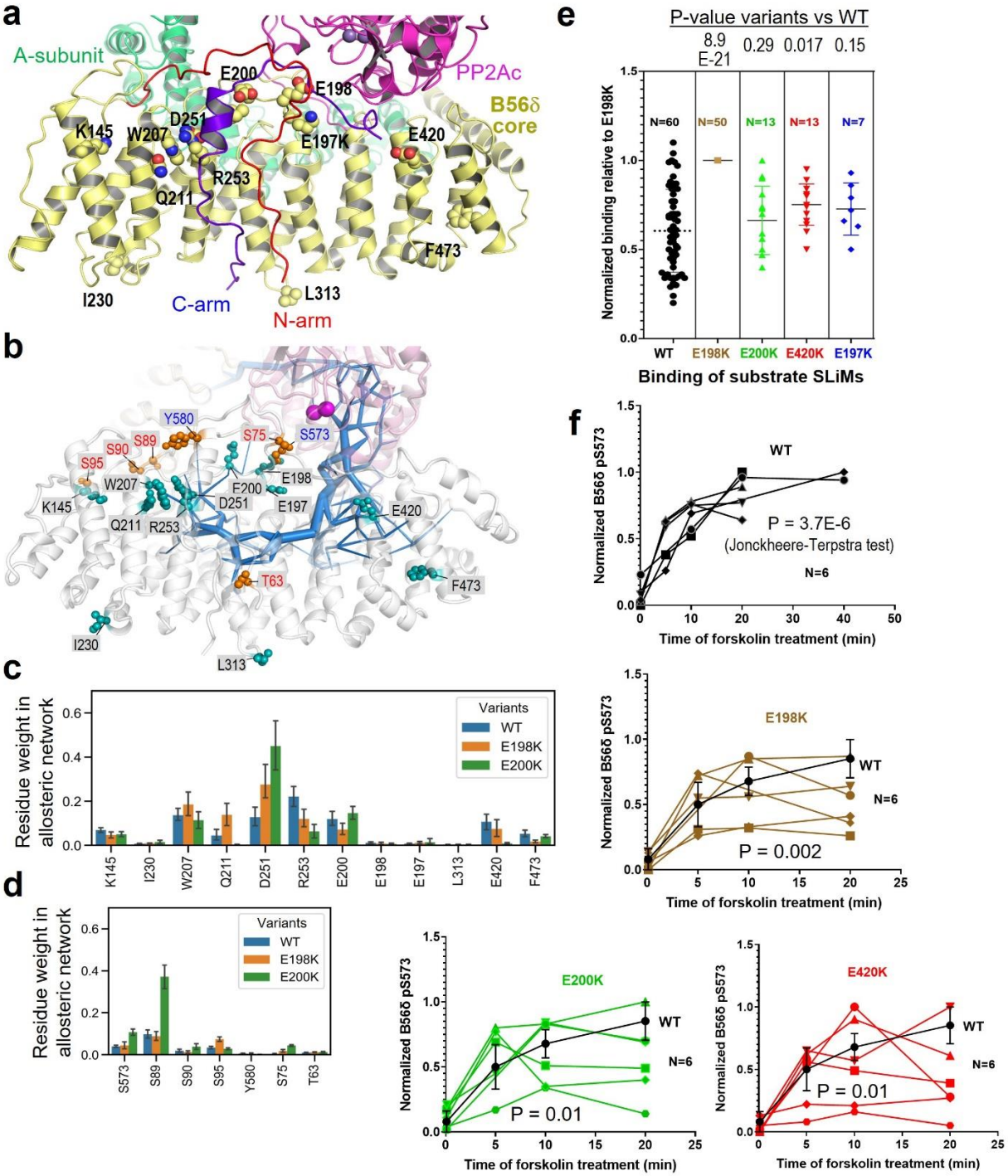

Figure 5. The allosteric network of the PP2A-B56δ holoenzyme, perturbation by B56δ ID mutations, and effects on holoenzyme functions. (a) Overall structure of the B56δ holoenzyme highlighting the B56δ ID residues that are predominantly located at the dynamic regulation interface. (b) Illustration of allosteric network of the PP2A-B56δ holoenzyme and its relationship to ID residues (green ball-and-stick) and activation phosphorylation sites on N/C-arms (orange ball-and-stick). Allosteric weights are shown as the thickness of blue wires. The allosteric weights are estimated from REST2 simulations of the WT holoenzyme, modified from the cryo-

EM structure of the E197K holoenzyme in the closed form. (c-d) The global perturbation of residue weights of ID residues and activation phosphorylation sites on the allosteric network by E198K and E200K. (e) Effects of ID mutations on substrate SLiM binding were assessed by pulldown of WT and mutant holoenzymes by GST-tagged B56 SLiM in CREB (99-161). The data is normalized with the binding intensity of E198K. (f) Time-dependent phosphorylation of S573 in HEK293 cells with WT and CRISPR-edited B56δ mutants upon stimulation of cellular cAMP/PKA. The experiments were repeated at least five times. Means ± SEM was calculated for WT for comparison to disease variants. The P-values for time-dependent changes were calculated using Jonckheere-Terpstra test. The results in (b-d) are the average of 20 REST2 trajectories. For (e-f), the number of repeats, their scater plots, averages and SEM are shown. The P values for comparison of WT and disease variants are calculated using two-sided Wilcoxon Rank Sum test.

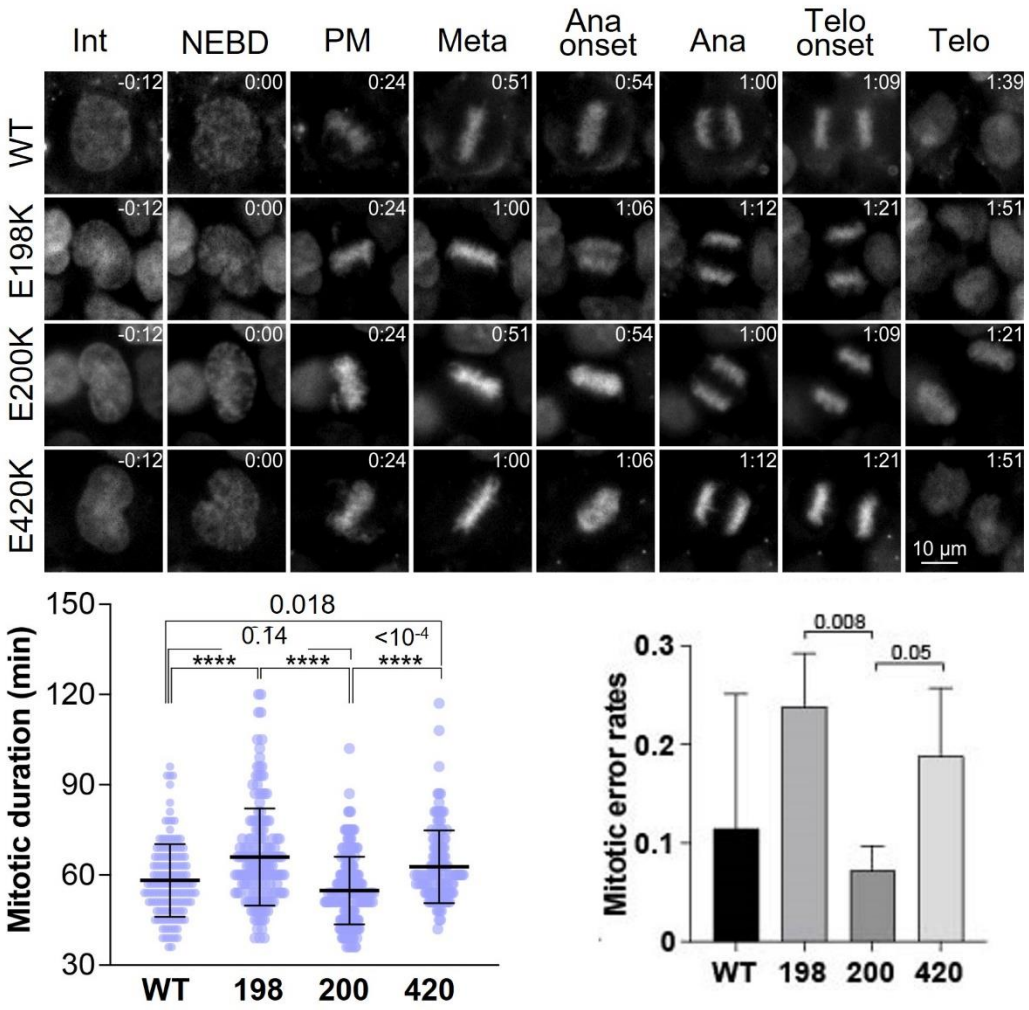

Figure 6. Effects of B56δ ID mutations on mitotic progression and mitotic errors. Representative live cell images of WT and B56δ ID mutant cells (E198K, E200K, and E420K) in HEK293 cells (top). Mitotic durations from NEBD to anaphase onset (bottom, left) and the frequency of mitotic errors (bottom, right) in above cells are plotted. The P values for comparison of WT and disease variants are calculated using One-Way Anova (bottom, left) and two-tailed t-test (bottom, right). P-values <0.0001 are indicated by "****".

Table 1 Cryo-EM data collection, refinement and validation statistics

PP2A-B56δ holoenzyme	WT close form by Spoiton	E197K close form
Data collection and processing		
Magnification (kx)	105	81
Voltage (kV)	300	300
Defocus (μm)	-1.2 to -2	-0.7 to -2.2
Pixel size (Å)	1.096	1.068
Total dose (e^- / $Å^2$)	66.84	49
Number of frames	50	69
Number of micrographs	1790	9158
Number of micrographs used	1534	7305
Number of initial particles picked	1,845,319	10,502,924
Number of final particles refined	40778	367,763
Map resolution (Å)	4.00	2.59
FSC threshold (Å)	0.143	0.143
Refinement		
Model cutoff (Å)	4.0	2.7
Total number of atoms	10136	11036
Map sharpening B factor ($Å^2$)	73.1	97.9
RMSD		
bond length ($Å^2$)	0.007	0.005
bond angle (°)	0.897	0.610
CC	0.79	0.85
Validation		
MolProbity Score	2.55	1.60
Clash score	33.70	6.88
Ramachandran plot (%)		
Favored	90.33	96.56
Allowed	9.68	3.44
Disallowed	0	0

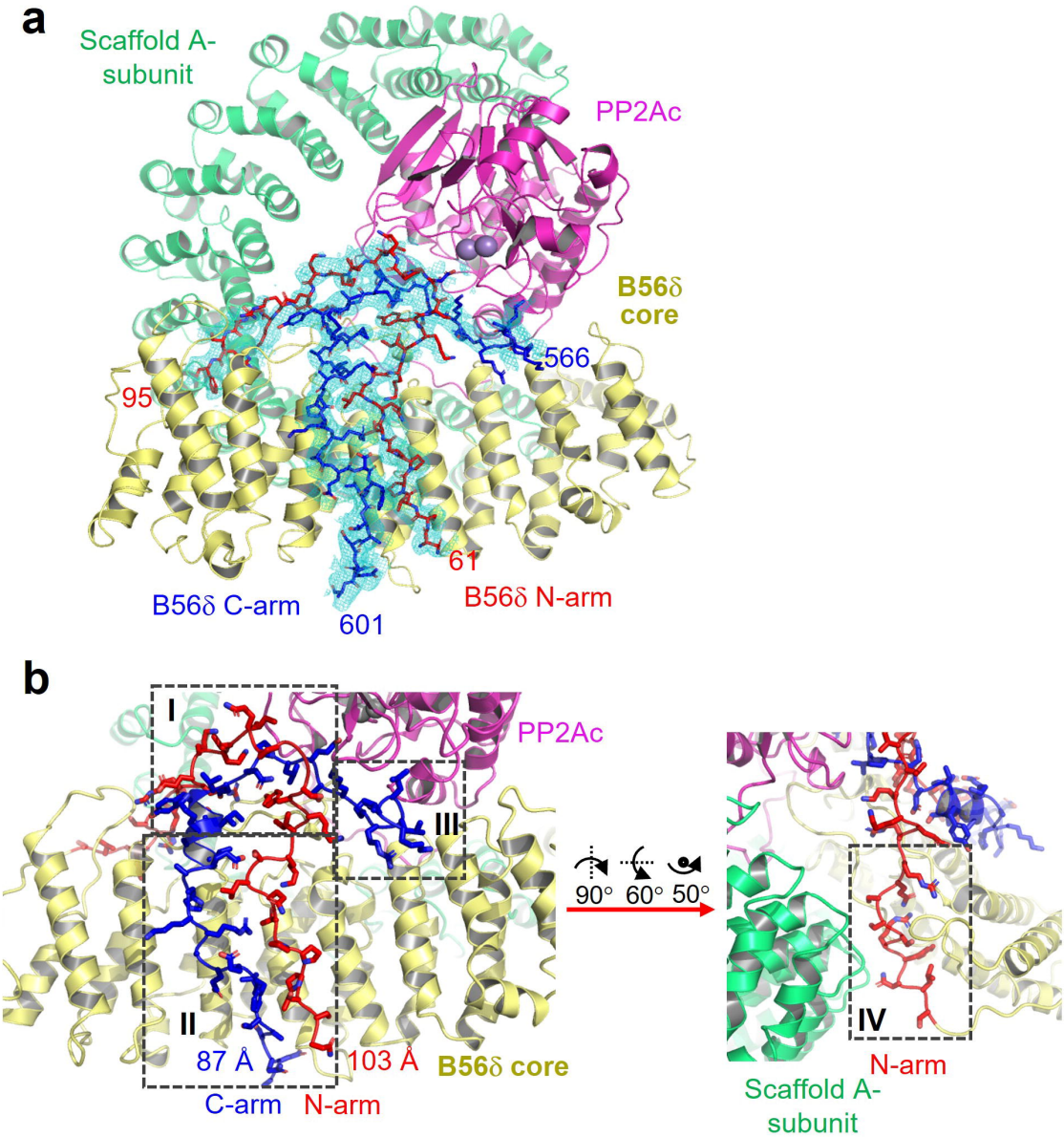

I: N/C-arm crossover-PP2Ac-B56-IL

	N/C	N-PP2Ac	C-PP2Ac	N-IL	C-IL
H-bonds	8	2	4	2	2
Hydrophobic	1	1			
salt bridge					1
unfavorable	1			2	2

II: N/C-arm-B56 core

	N/C	N-Core	C-Core-IL
H-bonds	3	4	8
Hydrophobic	5	2	5
salt bridge			
unfavorable			1

III: C-arm-PP2Ac-B56 core & IL

	C-PP2Ac	C-Core	C-IL
H-bonds		1	2
Hydrophobic	5	1	
salt bridge		1	1
unfavorable			

IV: N-arm-A-subunit-B56 core

	N-A	N-Core
H-bonds	3	8
Hydrophobic		3
salt bridge		1
unfavorable		2

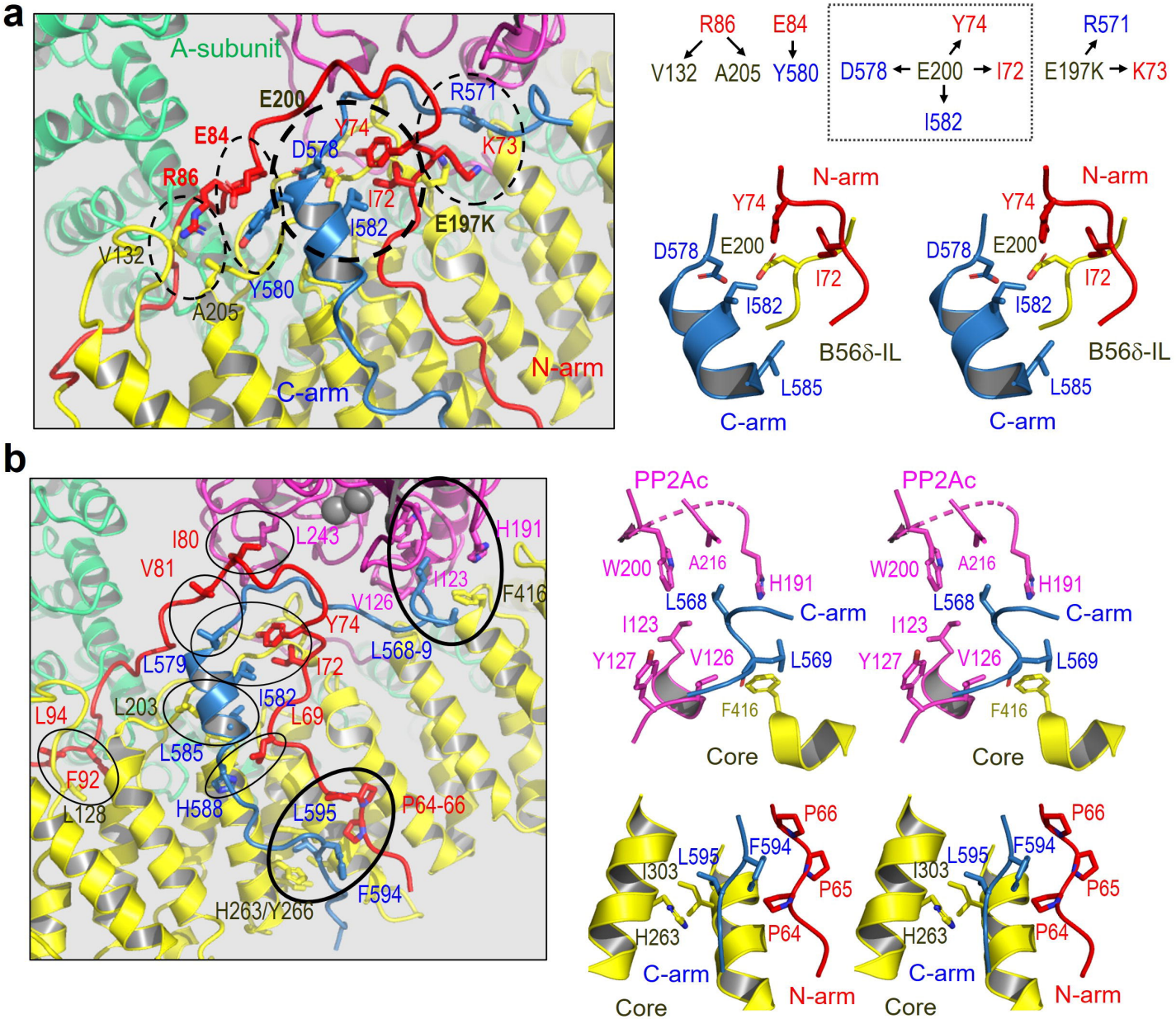
a
A-subunit
E200
E84
R86
R571
Y74
D578
K73
I72
I582
E197K
V132
Y580
A205
N-arm
C-arm
R86
E84
Y74
R571
V132
A205
Y580
D578
E200
I72
E197K
K73
I582
N-arm
Y74
D578
E200
I72
I582
B56δ-IL
L585
C-arm
N-arm
Y74
D578
E200
I72
I582
B56δ-IL
L585
C-arm
b
I80
L243
H191
V81
I123
F416
V126
Y74
L568-9
L579
I72
L203
I582
L69
L94
L585
F92
L128
H588
L595
P64-66
F594
H263/Y266
PP2Ac
W200
A216
H191
L568
C-arm
I123
Y127
V126
L569
F416
Core
PP2Ac
W200
A216
H191
L568
C-arm
I123
Y127
V126
L569
F416
Core
P66
L595
F594
I303
P65
H263
P64
C-arm
N-arm
Core
P66
L595
F594
I303
P65
H263
P64
C-arm
N-arm
Core

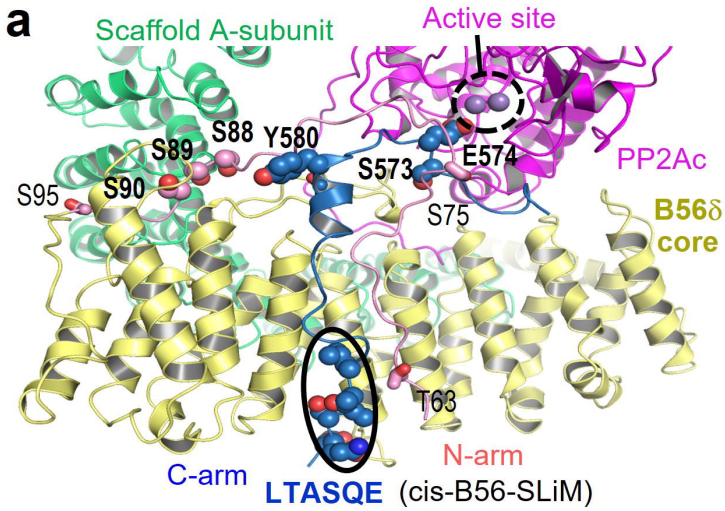

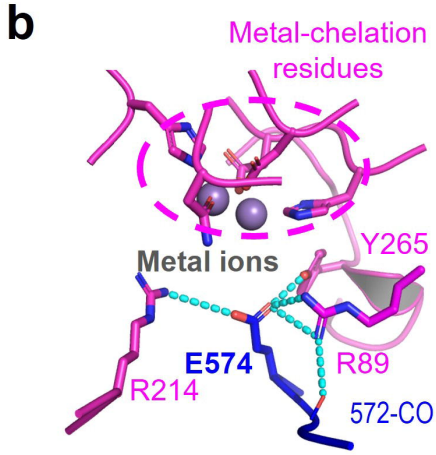

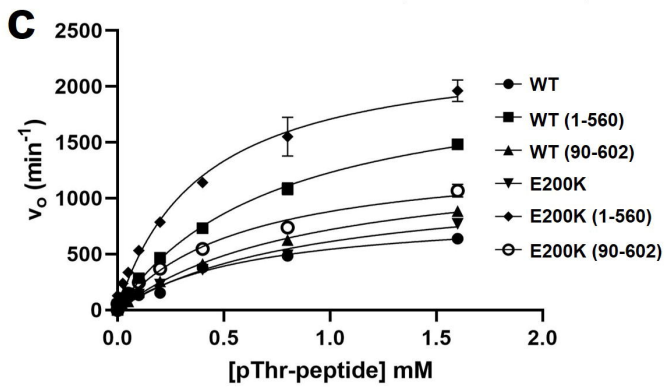

	WT FL	WT 1-560	WT 90-602	E200K FL	E200K 1-560	E200K 90-602
kcat	822 ± 71	2149 ± 125	1375 ± 85	1166 ± 207	2376 ± 224	1394 ± 181
Km	0.68 ± 0.13	0.74 ± 0.09	0.91 ± 0.12	0.90 ± 0.08	0.39 ± 0.13	0.60 ± 0.18

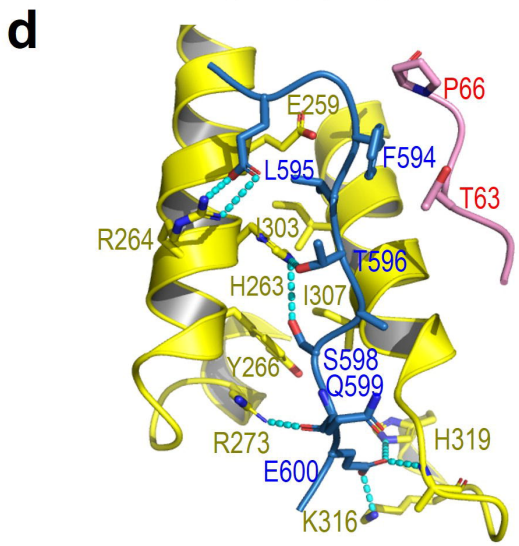

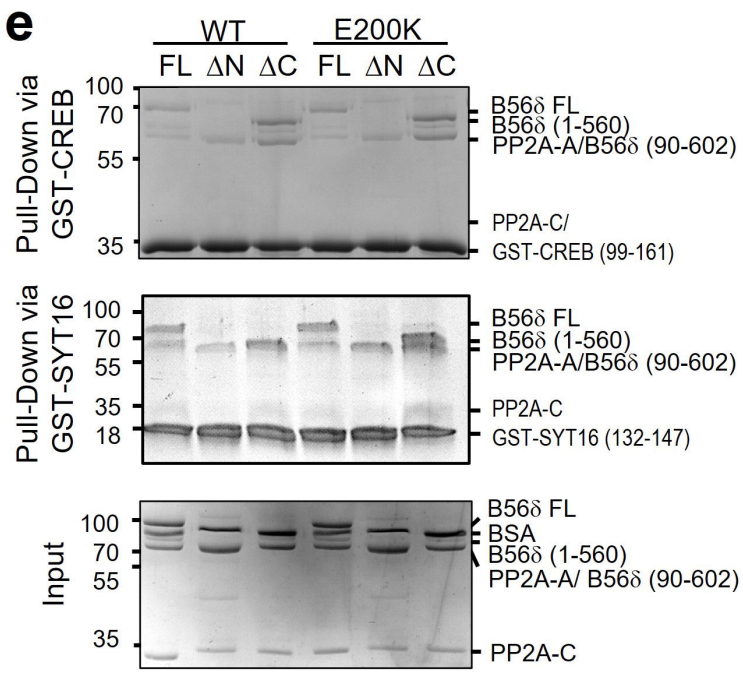

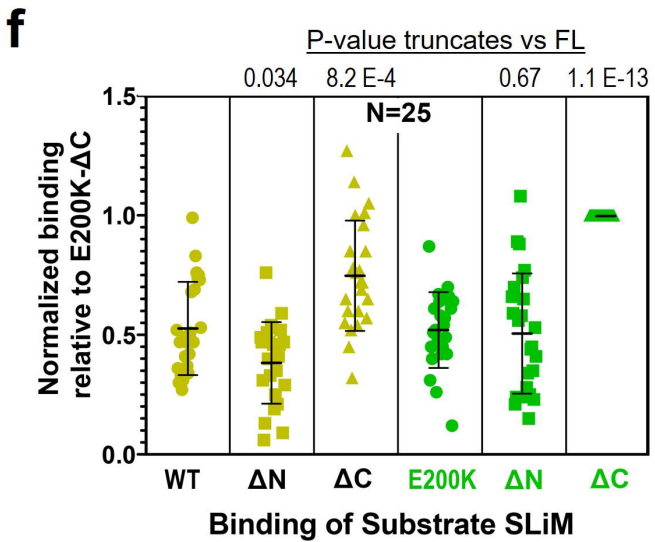

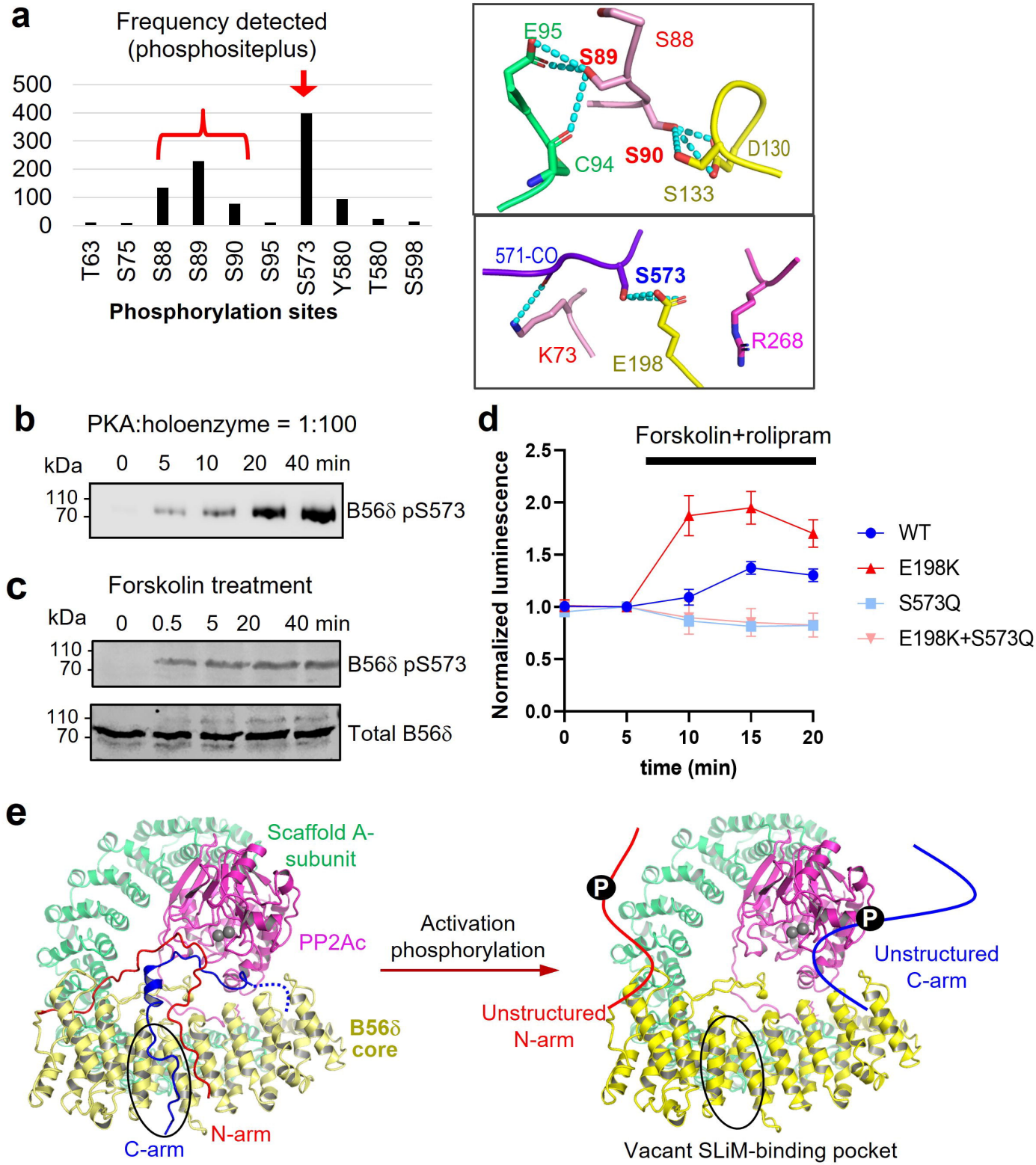
a
Frequency detected
(phosphositeplus)
500
400
300
200
100
0
T63
S75
S88
S89
S90
S95
S573
Y580
T580
S598
Phosphorylation sites
E95
S89
S88
C94
S90
D130
S133
571-CO
S573
K73
E198
R268
b
PKA:holoenzyme = 1:100
kDa
0
5
10
20
40 min
110
70
B56δ pS573
c
Forskolin treatment
kDa
0
0.5
5
20
40 min
110
70
B56δ pS573
110
70
Total B56δ
d
Forskolin+rolipram
Normalized luminescence
2.5
2.0
1.5
1.0
0.5
0.0
0
5
10
15
20
time (min)
WT
E198K
S573Q
E198K+S573Q
e
Scaffold A-
subunit
PP2Ac
B56δ
core
C-arm
N-arm
Activation
phosphorylation
P
P
Unstructured
C-arm
Unstructured
N-arm
Vacant SLiM-binding pocket

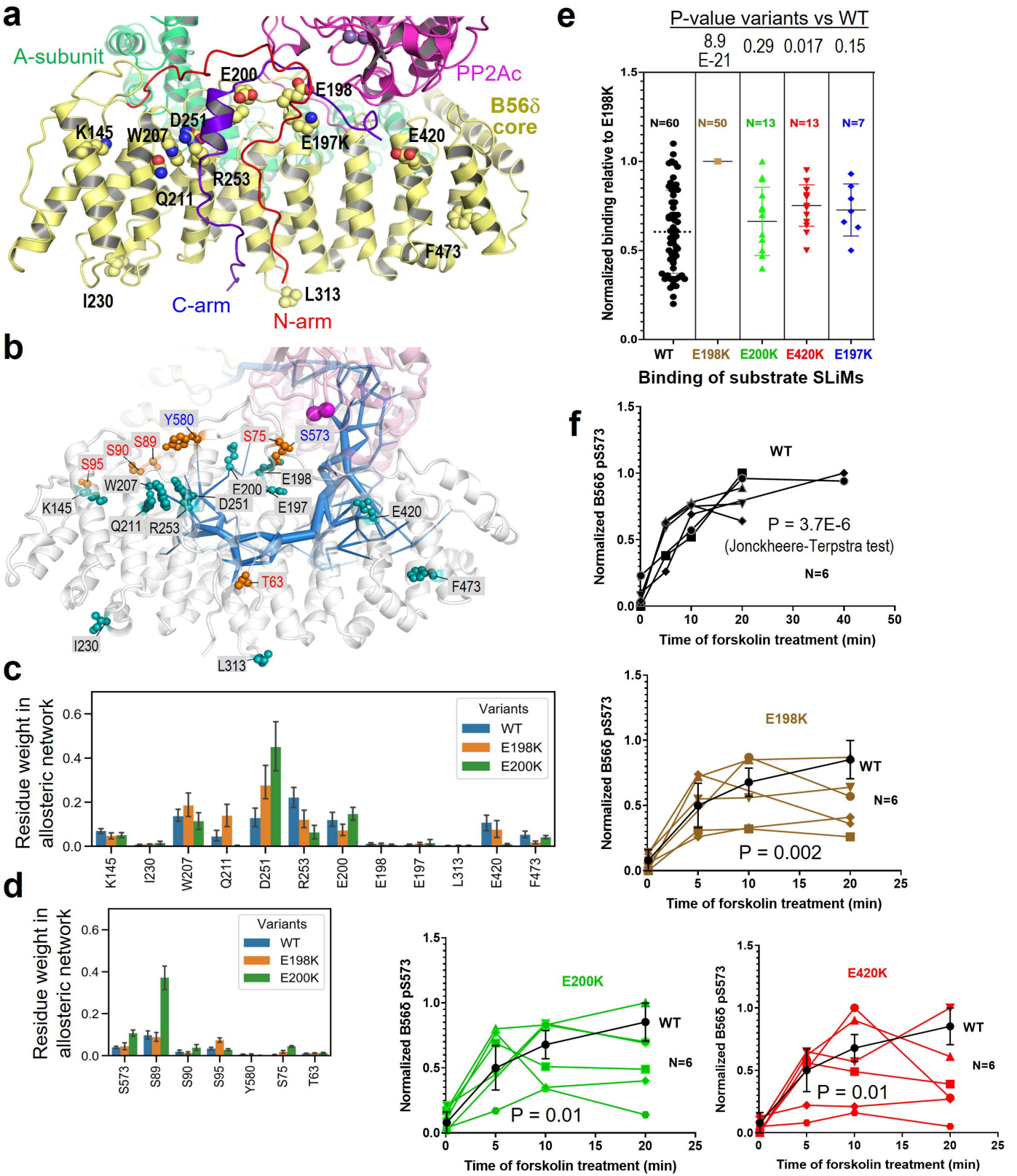
a
A-subunit
E200
E198
PP2Ac
B56δ core
K145
W207
D251
E197K
E420
R253
Q211
F473
I230
C-arm
L313
N-arm
b
Y580
S75
S573
S90
S89
S95
W207
E200
E198
K145
D251
E197
E420
Q211
R253
T63
F473
I230
L313
c
Residue weight in allosteric network
Variants
WT
E198K
E200K
K145
I230
W207
Q211
D251
R253
E200
E198
E197
L313
E420
F473
d
Residue weight in allosteric network
Variants
WT
E198K
E200K
S573
S89
S90
S95
Y580
S75
T63
e
P-value variants vs WT
8.9 E-21
0.29
0.017
0.15
Normalized binding relative to E198K
N=60
N=50
N=13
N=13
N=7
WT
E198K
E200K
E420K
E197K
Binding of substrate SLiMs
f
Normalized B56δ pS573
WT
P = 3.7E-6
(Jonckheere-Terpstra test)
N=6
Time of forskolin treatment (min)
E198K
WT
N=6
P = 0.002
E200K
WT
N=6
P = 0.01
E420K
WT
N=6
P = 0.01

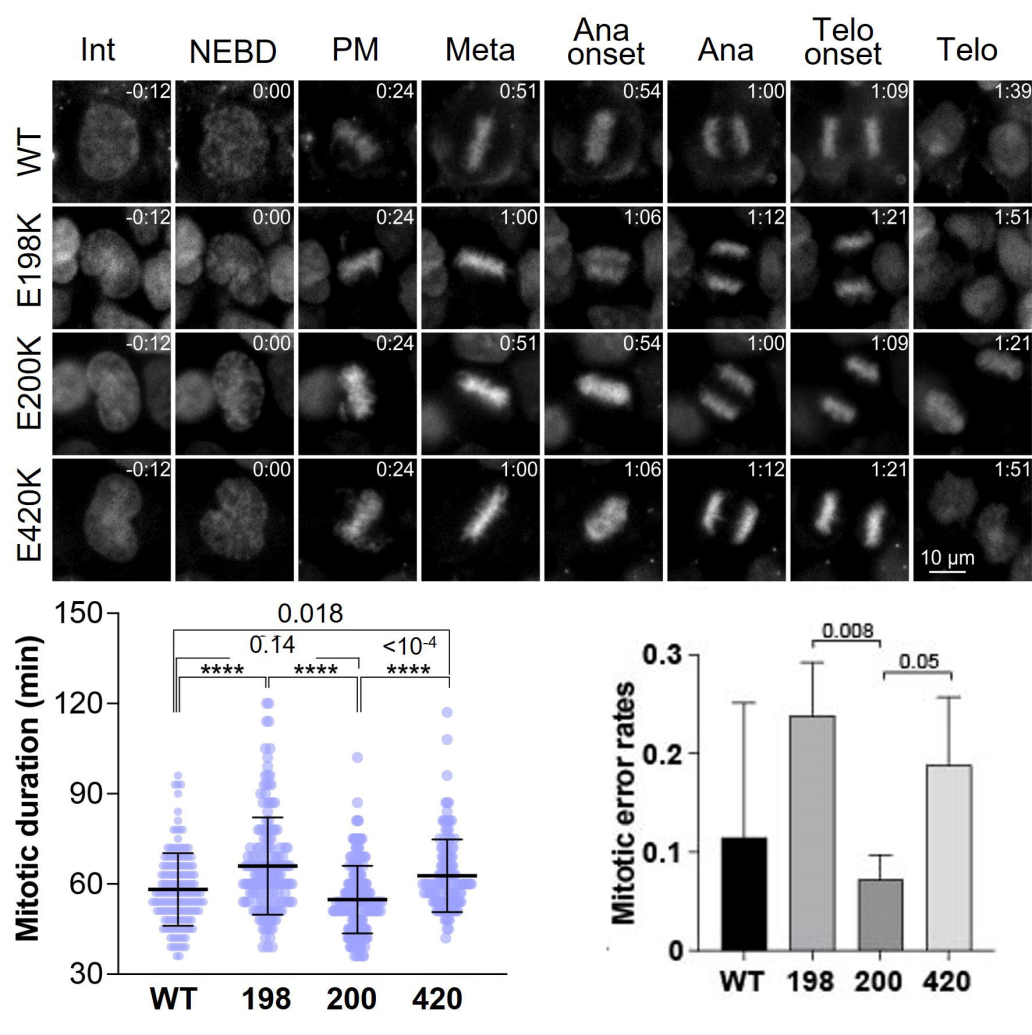
Int
NEBD
PM
Meta
Ana onset
Ana
Telo onset
Telo
WT
E198K
E200K
E420K
-0:12
0:00
0:24
0:51
0:54
1:00
1:09
1:39
1:06
1:12
1:21
1:51
10 µm
Mitotic duration (min)
150
120
90
60
30
0.018
0.14
<10-4
****
WT
198
200
420
Mitotic error rates
0.3
0.2
0.1
0
0.008
0.05